Numerical assessment of bed-load discharge formulations for transient flow in 1D and 2D situations

Carmelo Juez, Javier Murillo and Pilar García-Navarro

ABSTRACT

Two-dimensional (2D) transient flow over an erodible bed can be modelled using shallow-water equations and the Exner equation to describe the morphological evolution of the bed. Considering the fact that well-proven capacity formulae are based on one-dimensional (1D) experimental steady flows, the assessment of these empirical relations under unsteady 1D and 2D situations is important. In order to ensure the reliability of the numerical experimentation, the formulation has to be general enough to allow the use of different empirical laws. Moreover, the numerical scheme must handle correctly the coupling between the 2D shallow-water equations and the Exner equation under any condition. In this work, a finite-volume numerical scheme that includes these two main features will be exploited here in 1D and 2D laboratory test cases. The relative performances of Meyer-Peter and Müller, Ashida and Michiue, Engelund and Fredsoe, Fernandez Luque and Van Beek, Parker, Smart, Nielsen, Wong and Camenen and Larson formulations are analysed in terms of the root mean square error. A new discretization of the Smart formula is provided, leading to promising predictions of the erosion/deposition rates. The results arising from this work are useful to justify the use of an empirical sediment bed-load discharge formula among the ones studied, regardless of the hydrodynamic situation.

Key words | bed-load sediment transport, Exner equation, finite-volume method, smart bed-load formulation, two-dimensional shallow water

Carmelo Juez
Javier Murillo (corresponding author)
Pilar García-Navarro
Fluid Mechanics,
LIFTEC,
University of Zaragoza,
50018 Zaragoza,
Spain
E-mail: *jmurillo@unizar.es*

NOTATION

A_g	Grass coefficient
d_m	median diameter
d_n	normal distance between cells centers
d_{90}, d_{30}	grain diameters for which 90 and 30% of the weight of a nonuniform sample are finer, respectively
g	acceleration due to gravity
h	water depth
h_L	water depth on the left side
h_R	water depth on the right side
n	Manning–Strickler coefficient
NE	number of cell edges
$n_{u,i}$	unit vector associated with the local velocity at each cell
n_x, n_y	normal components in x, y directions
p	porosity of the solid material
p_{bx}, p_{by}	pressure integral in x, y directions
q_s	bed-load discharge
q_{sx}, q_{sy}	sediment discharge in x, y directions
s	ratio between ρ_s and ρ_w S_{fx}, S_{fy} friction slope in x, y directions
S_{ox}, S_{oy}	bed slope in x, y directions
t	time
T_b	modulus of bed shear stress
u, v	depth-averaged velocity in x, y directions
x, y	spatial coordinates of two dimensions in plane
z	bed elevation
z_L	bottom height on the left side
z_R	bottom height on the right side
δz	difference of bottom heights
θ	Shields parameter

doi: 10.2166/hydro.2013.153

θ_c critical Shields parameter
θ_c^S critical Shields parameter for Smart formula
ρ_s solid density
ρ_w water density
τ_{bx}, τ_{by} bed shear stress in x, y directions
φ friction angle
Φ dimensionless bed-load discharge

INTRODUCTION

When numerically modelling free-surface flows with load transport over an erodible bed, a closure formula is required for solving the bed-load transport if the shallow-water and Exner equations are employed. Several sediment transport capacity formulae are available in specialized literature (Meyer-Peter & Müuller 1948; Ashida & Michiue 1972; Engelund & Fredsoe 1976; Luque & van Beek 1976; Parker 1979; Smart 1984; Nielsen 1992; Wong 2003; Camenen & Larson 2005), each one arising from different laboratory and field data sets and developed for a limited range of conditions. As they have been based on one-dimensional (1D) steady sediment transport experiments, their performance must be analysed to ensure a correct assessment of the sediment transport rates for more complex and realistic unsteady 1D and two-dimensional (2D) situations. These empirical formulae, despite having been developed for predicting sediment transport in alluvial channels, have been extended to a wider field of scientific work (Campisano *et al.* 2004; Creaco & Bertrand-Krajewski 2009).

Conventional methods based on the shallow-water and Exner equations decouple the hydrodynamic part and the morphodynamic equation (Cunge *et al.* 1980; De Vriend *et al.* 1993; Abderrezzak & Paquier 2011). Hudson & Sweby (2002) studied 1D numerical solutions of the equations governing bed-load sediment transport following a completely coupled formulation, proving that this option is able to handle correctly the full range of hydrodynamic and morphodynamic problems, especially rapidly varying flows, for which decoupled formulations are not well suited. More recently, the improvement of computer technology has allowed the reformulation of the earliest 1D models into more sophisticated ones, making possible 2D computation of the flow behaviour and sediment transport possible (Cao *et al.* 2002; Wu & Wang 2004; Begnudelli & Sanders 2006).

Derivation of the numerical scheme in Hudson & Sweby (2002) relies on the use of the Grass sediment transport formula (Grass 1981). This sediment formula combines a global case-dependent calibration coefficient and a power law of the velocity. When extending this approximation to evaluate different empirical formulae, Castro Diaz *et al.* (2008) concluded that low-order numerical methods do not capture well the sediment evolution.

Following previous work (Rosatti *et al.* 2007), a generalized, well-balanced Roe solver in 2D was defined in Murillo & Garćıa-Navarro (2010). This Roe solver was able to extend the sediment transport formulation of Grass to general empirical sediment discharge formulae. In the same work, it was proved that the excessive numerical diffusion shown in Castro Diaz *et al.* (2008), associated with a low-order numerical scheme, can be avoided by using appropriate definitions for Roe's averaged variables.

This proposed numerical scheme (Murillo & García-Navarro 2010) was tested using exact solutions over a movable bed so that the method was able to predict faithfully the overall behaviour of the solution and of any type of wave. These characteristics make the numerical scheme an adequate tool to test the ability of well-proven capacity formulae under a complete set of experimental configurations. The present work is focused on verifying if the quality of the results is compromised by the simplicity of the closure formula, as was studied in Liu *et al.* (2008). This justifies the need of a systematic tool to analyse in depth the opportunities offered by the different formulae.

In this work, making use of the above numerical scheme, the relative performances of well-known sediment transport formulae have been analysed and, in addition, a new interpretation of the Smart (1984) empirical law is presented in order to cope with bed-load transport over irregular beds of changing slope. Detailed results for this new modified empirical law, together with the ones obtained by Meyer-Peter & Müller (1948) (which is the sediment capacity formula frequently used), are provided for every test case analysed. Furthermore, the root mean square errors (RMSEs) associated with every formula at each experimental condition are calculated for the purpose of evaluating quantitatively the overall behaviour of each

formulation. In this fashion, the outline of this paper is as follows: the mathematical description of the problem is described, and then the numerical scheme is presented following a new interpretation of the Smart formula. Next, the relative performance of the different closure formulations is tested against experimental data in different laboratory situations. Finally, conclusions are presented.

MATHEMATICAL MODEL

The system of equations used in this work is obtained by coupling the 2D mass and momentum shallow-water equations and the 2D Exner equation, neglecting suspension terms. This set of equations is written as follows:

$$\frac{\partial(h)}{\partial t}+\frac{\partial(hu)}{\partial x}+\frac{\partial(hv)}{\partial y}=0$$

$$\frac{\partial(hu)}{\partial t}+\frac{\partial[hu^2+(1/2)gh^2]}{\partial x}+\frac{\partial(huv)}{\partial y}=\frac{p_{bx}}{\rho_{\mathrm{w}}}-\frac{\tau_{bx}}{\rho_{\mathrm{w}}}$$

$$\frac{\partial(hu)}{\partial t}+\frac{\partial(huv)}{\partial x}+\frac{\partial[hv^2+(1/2)gh^2]}{\partial y}=\frac{p_{by}}{\rho_{\mathrm{w}}}-\frac{\tau_{by}}{\rho_{\mathrm{w}}}$$

$$\frac{\partial z}{\partial t}+\xi\frac{\partial q_{sx}}{\partial x}+\xi\frac{\partial q_{sy}}{\partial y}=0 \tag{1}$$

with (u, v) the depth-averaged components of the velocity vector along the (x, y) coordinates, h the water depth, z the bed elevation, g the acceleration due to gravity, $\xi=\frac{1}{1-p}$ with p the material porosity and q_{sx} and q_{sy} the solid transport unit discharge along the (x, y) coordinates. The terms corresponding to the right-hand side of the equations express the x-component and y-component of: (i) the pressure force along the bottom line, p_{bx} and p_{by}, with ρ_{w} the water density, which in differential form are expressed as a function of the bed slope, S_o:

$$\begin{aligned}\frac{p_{bx}}{\rho_{\mathrm{w}}}&=ghS_{ox} \quad S_{ox}=-\frac{\partial z}{\partial x}\\ \frac{p_{by}}{\rho_{\mathrm{w}}}&=ghS_{oy} \quad S_{oy}=-\frac{\partial z}{\partial y}\end{aligned} \tag{2}$$

and (ii) the bed shear-stress integral, τ_{bx} and τ_{by}, which written in terms of the Manning–Strickler coefficient n can be expressed as:

$$\begin{aligned}\frac{\tau_{bx}}{\rho_{\mathrm{w}}}&=ghS_{fx} \quad S_{fx}=\frac{n^2u\sqrt{u^2+v^2}}{h^{4/3}}\\ \frac{\tau_{by}}{\rho_{\mathrm{w}}}&=ghS_{fy} \quad S_{fy}=\frac{n^2v\sqrt{u^2+v^2}}{h^{4/3}}\end{aligned} \tag{3}$$

The bed-load discharge is assumed to follow the Grass formulation Grass (1981):

$$|\mathbf{q}_s|=\sqrt{q_{sx}^2+q_{sy}^2}=A_g|\mathbf{u}|^3 \tag{4}$$

with:

$$q_{sx}=A_gu(u^2+v^2) \qquad q_{sy}=A_gv(u^2+v^2) \tag{5}$$

where, following Murillo & García-Navarro (2010), A_g is not a constant, but takes values according to different empirical formulations for sediment transport.

The sediment discharge can be expressed through the following dimensionless parameter:

$$\Phi=\frac{|\mathbf{q}_s|}{\sqrt{g(s-1)d_{\mathrm{m}}^3}} \tag{6}$$

where $s=\rho_{\mathrm{s}}/\rho_{\mathrm{w}}$ is the ratio between solid material (ρ_{s}) and water densities, and d_{m} is the median diameter of the sediment material. Table 1 collects the formulae tested in this work, where d_{90} and d_{30} are the grain diameters for which 90 and 30% of the weight of a non-uniform sample are finer, respectively, θ_{c} is the critical Shields parameter, summarized in Table 1, $\theta_{\mathrm{c}}^{\mathrm{S}}$ is the critical Shield parameter expressed as Smart (1984).

The dimensionless bed shear stress or Shields parameter, θ, can be expressed as:

$$\theta=\frac{|\mathbf{T}_{\mathrm{b}}|}{g(\rho_{\mathrm{s}}-\rho_{\mathrm{w}})d_{\mathrm{m}}} \tag{7}$$

where $\mathbf{T}_b=(\tau_{bx}, \tau_{by})$ is the bed shear stress written as in (3):

$$|\mathbf{T}_{\mathrm{b}}|=\sqrt{\tau_{bx}^2+\tau_{by}^2}=\sqrt{(\rho_{\mathrm{w}}ghS_{fx})^2+(\rho_{\mathrm{w}}ghS_{fy})^2} \tag{8}$$

Table 1 | Summary of sediment formulae, particularized Grass coefficient and critical Shield parameter for sediment formulae

Formula	Φ	K_1	θ_c
Meyer-Peter & Müller (1948) (MPM in the text)	$8\ (\theta-\theta_c)^{3/2}$	$8\,(1-\theta_c/\theta)^{3/2}$	0.0470
Ashida & Michiue (1972)	$17\ (\theta-\theta_c)(\sqrt{\theta}-\sqrt{\theta_c})$	$17\ (1-\theta_c/\theta)(1-\sqrt{\theta_c/\theta})$	0.0500
Engelund & Fredsoe (1976)	$18.74\ (\theta-\theta_c)(\sqrt{\theta}-0.7\sqrt{\theta_c})$	$18.74\ (1-\theta_c/\theta)(1-0.7\sqrt{\theta_c/\theta})$	0.0500
Fernandez Luque & Van Beek (1976)	$5.7\ (\theta-\theta_c)^{3/2}$	$5.7\ (1-\theta_c/\theta)^{3/2}$	0.037–0.0455
Parker (1979) fit to Einstein (1950)	$11.2\ (1-\theta/\theta_c)^{9/2}$	$11.2\ (1-\theta/\theta_c)^{9/2}$	0.030
Smart (1984)	$4\ (d_{90}/d_{30})^{0.2}\ S^{0.6}\ C\theta^{1/2}(\theta-\theta_c^S)$	$4\ (d_{90}/d_{30})^{0.2}\ S^{0.6}\ C(1-\theta_c/\theta)$	0.0470
Nielsen (1992)	$12\ \theta^{1/2}(\theta-\theta_c)$	$12\ (1-\theta_c/\theta)$	0.0470
Wong (2003) (Wong (4.93) in the text)	$4.93\ (\theta-\theta_c)^{1.6}$	$4.93\,(1-\theta_c/\theta)^{3/2}\,(\theta-\theta_c)^{0.1}$	0.0470
Wong (2003) (Wong (3.97) in the text)	$3.97\ (\theta-\theta_c)^{3/2}$	$3.97\,(1-\theta_c/\theta)^{3/2}$	0.0495
Camenen & Larson (2005)	$12\ \theta^{3/2}\exp(-4.5\theta_c/\theta)$	$12\ \exp(-\theta/\theta_c)$	0.0400

When inserting (8) in (7), the dimensionless shear stress is written as a function of the friction slope, $\theta=\theta(S_f)$:

$$\theta=\frac{n^2}{(s-1)d_m h^{1/3}}(u^2+v^2)=\frac{n^2}{(s-1)d_m h^{1/3}}|\mathbf{u}|^2 \tag{9}$$

Using (4) and (6), and bearing in mind (7)–(9), the empirical transport formulae have been expressed as:

$$|\mathbf{q}_s|=K_0\,K_1\,(u^2+v^2)^{3/2}=A_g|\mathbf{u}|^3 \tag{10}$$

with $A_g=K_0\,K_1$, $K_0=\frac{g^{1/2}n^3}{(s-1)h^{1/2}}$ and K_1 varying in each case as displayed in Table 1. Details can be found in Murillo & García-Navarro (2010).

NUMERICAL ALGORITHM

The computational method used to solve the coupled system in (1) is based on a finite-volume scheme, described in detail in Murillo & García-Navarro (2010). This method divides the domain in computational cells using a mesh fixed in time. The Gauss theorem is applied to each volume cell allowing the computation of the liquid and solid flux through the edges of each cell. Each variable is updated using an explicit first order in space finite-volume scheme. The allowable time step sizes are controlled by the Courant–Friedrich–Lewy condition (Murillo & García-Navarro 2010).

The model is well balanced and allows a stable computed solution under all ranges of hydrodynamic and morphodynamic problems, avoiding possible interferences between numerical modelling issues and sediment transport capacity formulation performance.

Slope formulation and discretization for the Smart model

The evaluation of $A_{g,i}$ at each cell is required along the simulation, and depends on the empirical formula used for bed-load transport. All the empirical formulations presented in Table 1 are written as a function of the friction slope through the Shields parameter, $\theta_i=\theta(S_{f,i})$, with:

$$S_{f,i}=n^2\frac{|\mathbf{u}_i|}{h_i^{4/3}} \tag{11}$$

The Smart formulation considers an additional factor, S. In the original contribution (Smart 1984), this term was based on an estimation of the bed slope along the preferential flow direction. When applying numerical modelling techniques, this term has often been evaluated (Tingsanchali & Chinnarasri 2001; Abderrezzak & Paquier 2011) using the friction slope in order to avoid undesirable results associated with flat bottoms, where the bed slope becomes null and consequently the sediment discharge is not available. The use of the friction slope in the sediment discharge formula is coherent with the fact that the

transport process implies a loss of energy through the interaction between the sediment and the flow (Whittaker & Davies 1982; Smart 1984).

The present work is concerned with the development of a 2D model that includes an extension of the Smart model for the bed-load discharge with a dynamical condition for the slope variable. In the 2D model, the bed slope is defined along the two horizontal coordinate directions. Considering that the Smart formula was derived from 1D experimental cases involving a constant bed slope in the flow direction, in a 2D simulation, it is necessary to define appropriate bed-slope estimations. The bed slope in the local flow direction, $|S_{o,\mathbf{u}}|$, is given by:

$$|S_{o\mathbf{u}}|_i = |\mathbf{S}_{oi}\mathbf{n}_{\mathbf{u}i}| = |\mathbf{S}_{o,i}\frac{\mathbf{u}_i}{|\mathbf{u}|_i}| \tag{12}$$

where $\mathbf{n}_{\mathbf{u},i}$ is the unit vector associated with the local velocity $\mathbf{u}$, i at each cell i and $\mathbf{S}_{o,i} = (S_{ox},\ S_{oy})$ is calculated through the slope at each k cell edge:

$$S_{ox} = \frac{-\left(\sum_{k=1}^{\mathrm{NE}}\left(\frac{\delta z\, n_x}{d_{\mathrm{n}}}\right)_k\right)}{\left(\sum_{k=1}^{\mathrm{NE}}|n_x|_k\right)} \quad S_{oy} = \frac{-\left(\sum_{k=1}^{\mathrm{NE}}\left(\frac{\delta z\, n_y}{d_{\mathrm{n}}}\right)_k\right)}{\left(\sum_{k=1}^{\mathrm{NE}}|n_y|_k\right)} \tag{13}$$

where NE is the number of cell edges, δz is the difference of bottom heights, d_{n} is the normal distance between the centres of cells and n_x, n_y are the components of the normal vector along the axis. Note that (13) can be used in both rectangular and triangular meshes.

In this work, the 2D formulation and discretization of the Smart model proposed is referred to as the Smart combined friction and bed slope (Smart CFBS):

$$S = \begin{cases} |S_{o,\mathbf{u}}|_i & \text{if } \mathbf{S}_{o,i}\mathbf{u}_i > 0 \\ S_{f,i} & \text{otherwise} \end{cases} \tag{14}$$

When using the friction slope under any morphodynamic condition, this option will be called Smart.

Geomorphological collapse

When managing transient geomorphological flows in realistic cases, the geotechnical equilibrium bank characteristics can be ruined, leading to dramatic channel metamorphosis. This effect needs to be modelled to reproduce correctly bed-geometry evolution in combination with flow action. In this work, the effect of the geomorphological collapse is introduced in the simulation by a simple mass conservative mechanism of slope sliding failure, assuming that the angle of repose of submerged material of the bed can be approximated by the friction angle. The failure mechanism is applied by comparison between the bed slope in each cell edge k, computed as $\delta z_k/d_{\mathrm{n}_k}$, and the angle of repose of saturated bed material (Murillo & Garćıa-Navarro 2010).

TEST CASES

Dam break flow over a mobile bed with a negative step (1D)

These experiments were performed in a flume designed at the Catholic University of Louvain (UCL) Civil Engineering Department by Spinewine & Zech (2007). The flume had a length of 6 m, 3 m on both sides of a central gate simulating an idealized dam. The channel width was set constant, equal to 25 cm. The bed material was coarse sand with the following properties: particle sizes ranging from 1.2 to 2.4 mm, with $d_{\mathrm{m}} = 1.82$ mm, density $\rho_{\mathrm{s}} = 2,683$ kg m^{-3}, a friction angle $\varphi = 30^{\circ}$, negligible cohesion, porosity $p = 0.47$, characterized by a Manning roughness factor $n = 0.0165$.

The regions upstream and downstream of the gate were filled with sediments (z_{L} and z_{R} respectively) and different water depths (h_{L} and h_{R}), as shown in Figure 1. The experimental data from two test cases have been compared with the numerical results. These two experiments differ only in

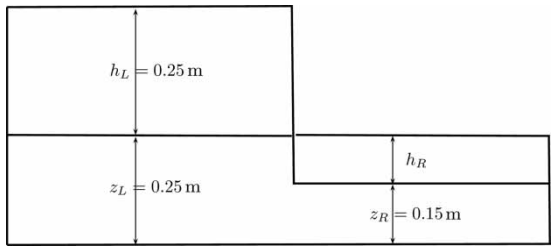

Figure 1 | Sketch of the dam break configuration.

the value of h_R. The first test case A ($h_R = 0$) has been chosen to guarantee the correct performance of the numerical scheme in combination with a sediment discharge formulation, in cases where morphological changes are produced in the presence of a dry bed. Case B ($h_R = 0.10$ m) allows checking if the numerical scheme in combination with a sediment discharge law is able to handle the different types of waves that may arise in a dam break case over a wet bed. Numerical simulations have been performed using $\Delta x = 0.01$ m. In all the simulations, the bed domain is considered deformable, and no boundary condition is imposed at the downstream section.

Test A

Test A corresponds to a reservoir partially filled with sediments and includes a downward step. Figure 2 shows the longitudinal bed and surface profiles calculated using the

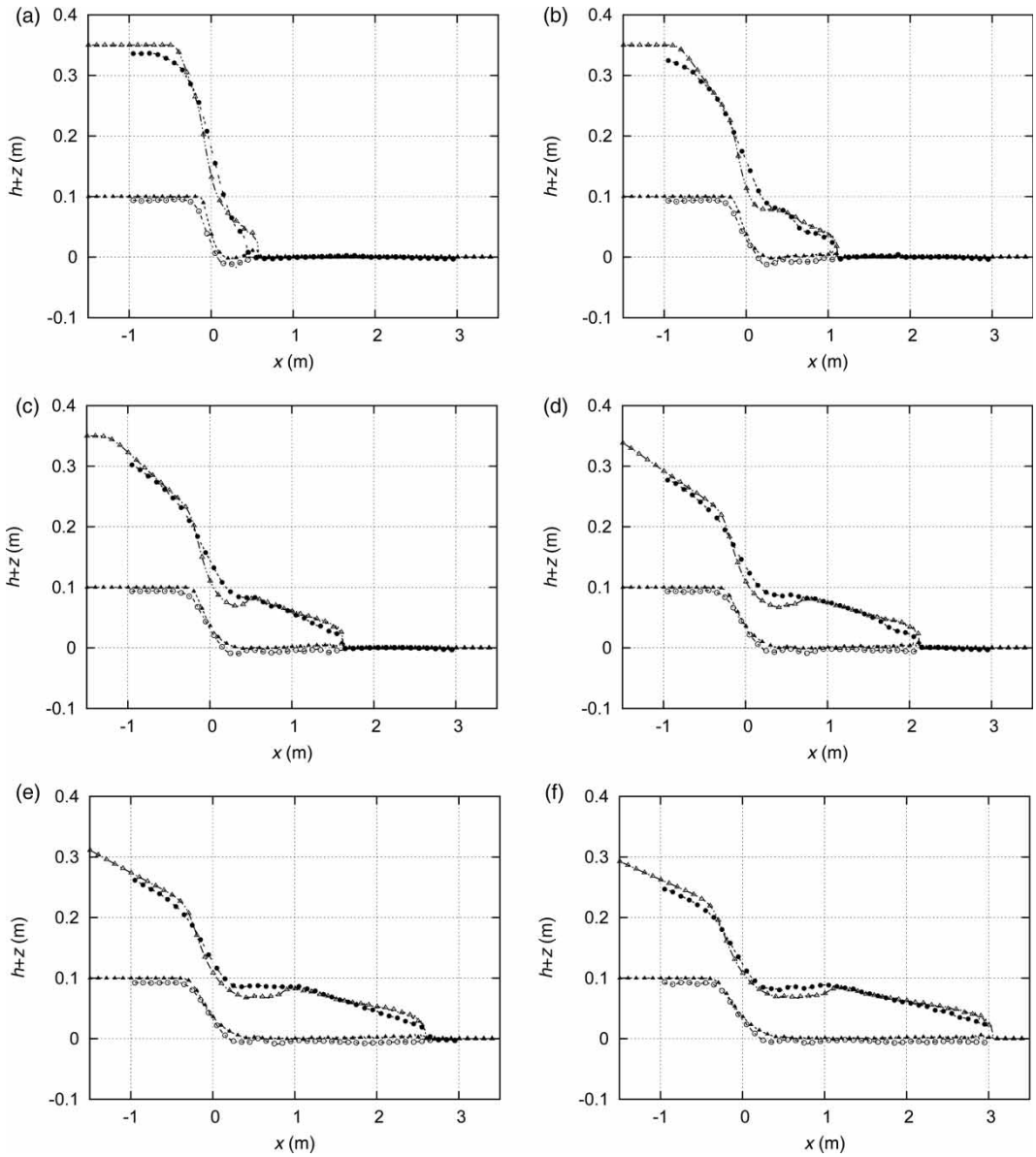

Figure 2 | Numerical results and experimental data for the dam break test case A at times $t = 0.025$ (a), 0.050 (b), 0.075 (c), 0.100 (d), 0.125 (e) and 1.5 s (f), using a variable value of A_g computed using Smart CFBS: measured water-level surface (– • –), measured bed-level surface (–○–), computed water-level surface (–△–), measured bed-level surface (–▲–).

Smart CFBS formulation and their accuracy in time. Free-surface and bed levels are correctly captured for both rarefaction waves and advance front waves, as well as the bed level at the discontinuity point.

Figure 3 shows numerical results and experimental data for the dam break using the Meyer-Peter–Müller (MPM) (left) and Smart CFBS (right) formulae at time $t = 1.5$ s. The main difference between both formulae appears at the step, where the MPM formula tends to underestimate the erosion process leading to a poor prediction of the bed level.

The RMSEs for water-level surfaces (left) and bed-level surfaces (right) displayed in Figure 4 show that the Smart CFBS formulation gives the best results, drastically reducing the error. The rest of the formulations provide a similar error. The Smart CFBS formula has the advantage of having been defined by the local flow conditions. For this particular case, where the bed slope is oriented in the flow direction, the term S_o in the Smart formula is evaluated as in (12) instead of using the traditional friction slope. This difference in the slope discretization provokes a noticeable difference in the RMSEs obtained when using the Smart and Smart CFBS formulae.

Test B

Test B is the case of a downward bed step combined with an initial layer of clear water in the downstream reach. The flow evolves in time, leading to a left moving rarefaction wave upstream of the gate, followed by a steady hydraulic jump downstream of the gate, and ending in a right moving shock.

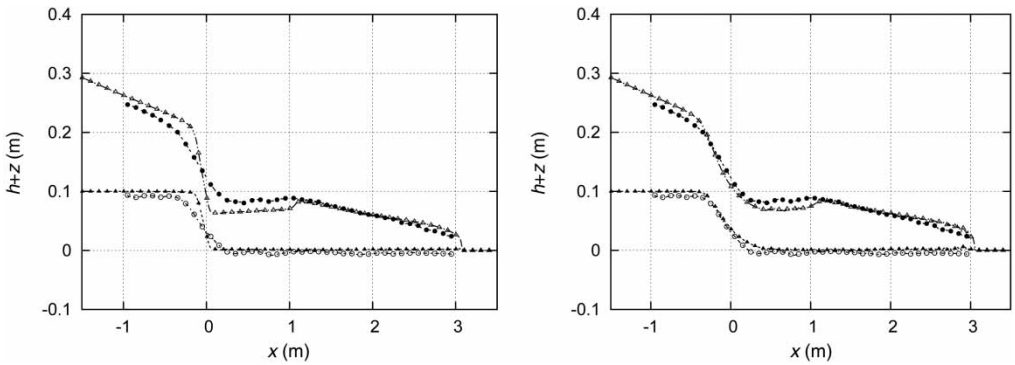

Figure 3 | Numerical results and experimental data for the dam break test case A at $t = 1.5$ s, using a variable value of A_g computed using MPM (left) and Smart CFBS (right): measured water-level surface (– • –), measured bed-level surface (–○–), computed water-level surface (–△–), measured bed-level surface (–▲–).

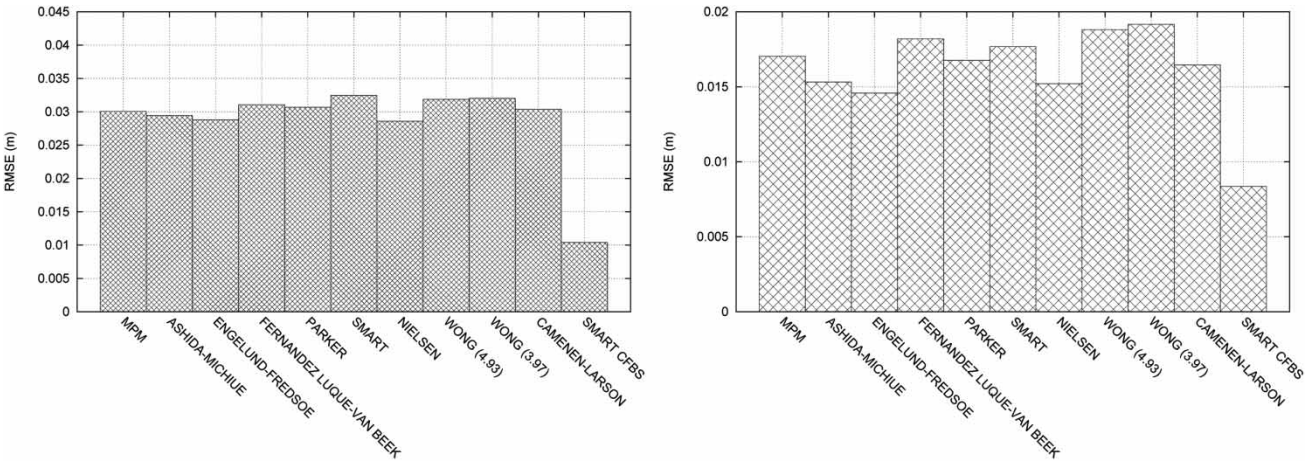

Figure 4 | RMSEs for water-level surface (left) and bed-level surface (right) with different formulae at $t = 1.5$ s in test A.

Figure 5 is a plot of free-surface and bed-level profiles at different times, where it can be observed how the shock celerity is perfectly captured by the numerical scheme in combination with the Smart CFBS formulation. Small differences produced in the shock wave are attributable to fast transient energy variations associated with the existence of a hydraulic jump.

Figure 6 gathers numerical results and experimental data using the MPM (left) and the Smart CFBS (right) formulae for direct comparison at time $t = 1.5$ s. The results obtained with the MPM formulae tend to inaccurately reduce the erosion transport over the step. This lack of precision in the bed-level prediction generates an incorrect estimation of the water-level surface in the hydraulic jump.

The Smart CFBS formula leads to the smallest error in comparison with the other discharge formulae, as shown in Figure 7 where the RMSEs for water-level surface (left) and bed-level surface (right) are displayed with different formulae

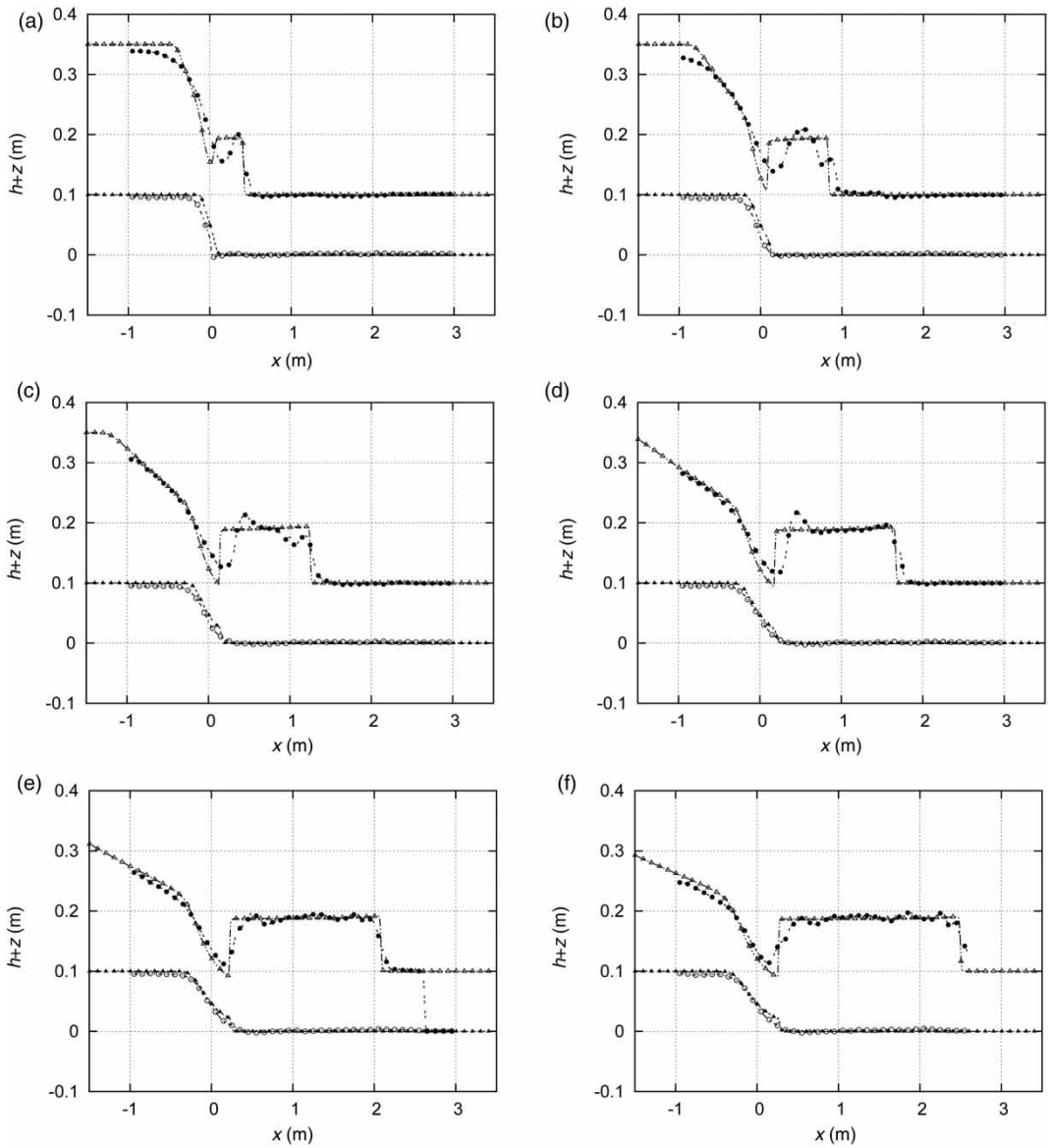

Figure 5 | Numerical results and experimental data for the dam break test case B at times $t = 0.025$ (a), 0.050 (b), 0.075 (c), 0.100 (d), 0.125 (e) and 1.5 s (f), using a variable value of A_g computed using Smart CFBS: measured water-level surface (– • –), measured bed-level surface (–○–), computed water-level surface (–△–), measured bed-level surface (–▲–).

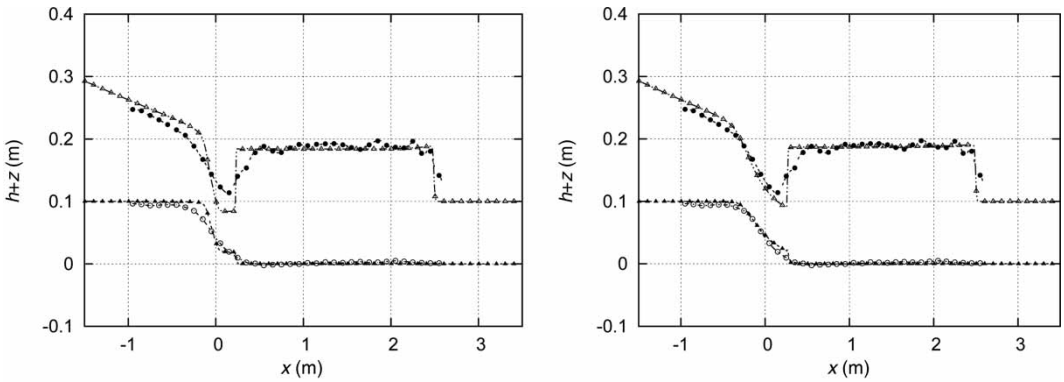

Figure 6 | Numerical results and experimental data for the dam break test case B at $t = 1.5$ s, using a variable value of A_g computed using MPM (left) and Smart CFBS (right): measured water-level surface (–•–), measured bed-level surface (–○–), computed water-level surface (–△–), measured bed-level surface (–▲–).

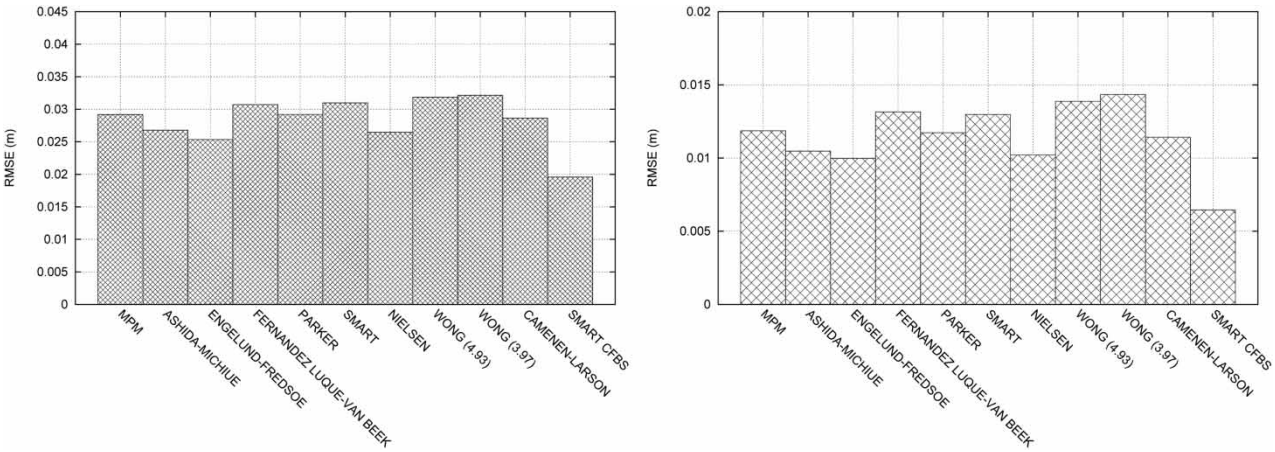

Figure 7 | RMSEs for water-level surface (left) and bed-level surface (right) with different formulae at $t = 1.5$ s in test B.

at $t = 1.5$ s. The RMSEs are quite similar among formulae, and the favourable advantage of the Smart CFBS formula over the traditional Smart formula is quite remarkable.

Dam erosion and failure, uniform overtopping

Dam surface erosion and slope sliding failure in time due to flow overtopping was studied by Tingsanchali & Chinnarasri (2001). Figure 8 shows a sketch of the experimental setup. Experiments were carried out in a rectangular flume 35 m long, 1.0 m deep and 1.0 m wide. The height and crest width of the dam were fixed at 0.80 and 0.30 m. The upstream slope was fixed at 1V:3H, while the downstream slope was set to 1:5. The dam was made of sand with the following characteristics: $\rho_s = 2{,}650\,\mathrm{kg\,m^{-3}}$, $d_{30} = 0.52$ mm, $d_m = 0.86$ mm, $d_{90} = 3.80$ mm and $d_m = 1.13$ mm. A friction angle of $\varphi = 30^\circ$ was suggested, and the porosity was estimated using the formula of Wu & Wang (2007), leading to $p = 0.22$. The Manning roughness coefficient was estimated to be equal to $n = 0.015$.

To have a uniform overflow across the flume width, in the experiment reproduced in this work, a vertical plate was held at the dam crest across the flume width until the upstream water level was 3 cm higher than the dam crest. The vertical plate was lifted up suddenly to allow the overflow to start.

Three zones can be distinguished. The first is a subcritical region in the reservoir area, characterized by a very low velocity. The second zone is a supercritical region of highly unsteady flow over a steep bed slope in the downhill slope of

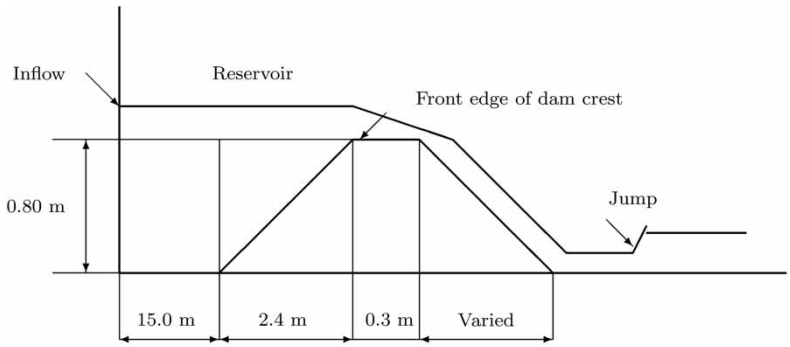

Figure 8 | Sketch of the dam failure experimental setup.

the dam, starting at the front edge of the dam crest. The third zone, downstream of the dam is characterized by the presence of a hydraulic jump. The dam erosion model was computed using $\Delta x = 0.05$ m.

During the development of this experiment, the bed level was recorded in time at three stations: SA, SB and SC, located respectively 15, 65 and 115 cm downstream from the front edge of the original dam crest. The overtopping discharge was also caught along time, as well as the reservoir level, just upstream of the breach. The results presented below compare experimental and computed data in order to validate the accuracy of the numerical method.

On the left-hand side of Figure 9, numerical results for water level and bed level using the Smart CFBS and MPM formulae are plotted. On the right-hand side of the figure, a plot shows measured and computed bed-level surface in time evolution at stations SA, SB and SC. Figure 10 displays, on the left, experimental and computed values of reservoir free-surface levels using Smart CFBS and MPM formulae. It can be observed how the computed results obtained with the new proposed formulation show a good agreement with the experimental data, while MPM predictions are quite far away from experimental data. On the right-hand side of Figure 10, a plot of the evolution in time of the overtopping discharge is depicted, and the maximum peak discharge reached with Smart CFBS agrees with the measured value. Differences in the shape of the discharge curve before and after the peak flow are in agreement with the bed-level evolution, computed and measured, obtaining more accurate results at the later instants of time, when most of the morphodynamic changes in the dam crest have occurred. On the other hand, the predictions obtained with the MPM formula lead to a poor estimation of the curve discharge.

As the prediction of the maximum discharge is of utmost importance in situations of dam failure, the maximum overtopping discharge achieved with the different formulae are presented in Figure 11. The continuous line at the top of the figure represents the maximum experimental overtopping discharge, which is only well calculated with the Smart CFBS formula. The rest of the formulae give values quite far away from the experimental value.

The relative performance of the different formulations in terms of RMSE is plotted in Figure 12 at the three stations SA, SB and SC, showing important differences among numerical results depending on the formula selected. The Engelund & Fredsoe sediment transport relation was derived for a wide range of slopes, and Figure 12 shows how this formulation leads to low values of RMSE. The Smart formula was derived for a set of experimental cases with steep slopes; therefore, it can be expected that in this case, any numerical approach of the term of the slope would provide accurate predictions. On the other hand, numerical simulation shows that the Smart discretization (considering that the slope term is included in the formula as the friction slope) leads to less accurate results if compared with those given by the Smart CFBS discretization. The rest of the formulations, derived from experiments ranging from low to medium slopes, provide higher RMSEs.

It has been considered important to check the performance of the numerical discretization of the empirical formulations in a triangular unstructured 2D mesh to analyse whether numerical results may be influenced by the

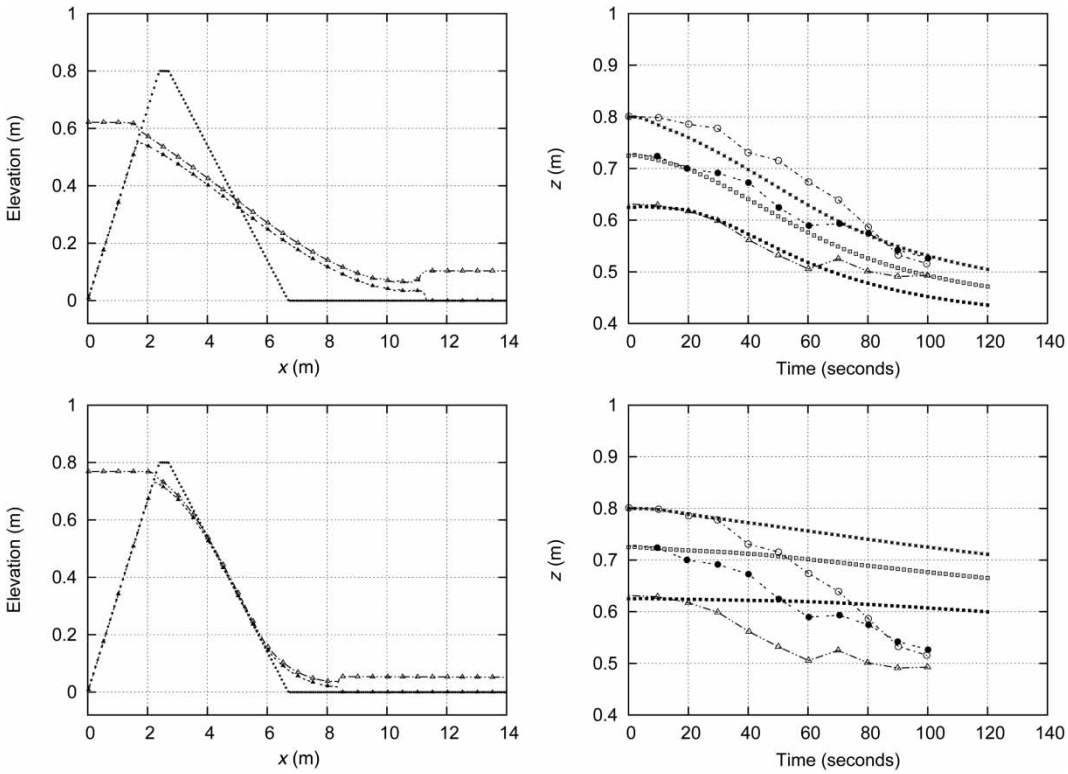

Figure 9 | Results obtained with Smart CFBS (upper) and MPM (lower) in the 1D case. Initial bed level (- - -), computed water-level surface (–△–) and bed-level surface –▲–) at $t = 120$ s (left). Bed-level surface evolution in time measured at stations SA (–○–), SB (– • –) and SC (–△–) and computed at stations SA (– ⋆ –), SB (–□–) and SC (–■–) (right).

grid definition under a wide variety of flow conditions. 2D numerical simulations have been developed using a coarse unstructured triangular mesh, with a maximum cell size of 0.01 m^2, as shown in Figure 13. The rest of the parameters are the same as the ones presented in the 1D test case.

The set of results presented in Figures 9 and 10 for a 1D mesh are repeated here in Figures 14 and 15 for a 2D mesh. The RMSEs for bed levels at stations SA, SB and SC with different formulae in time are plotted in Figure 16. This test case, with a finer mesh and comparing also with the MPM formula, has been discussed by Juez *et al.* (2012). From both results, it can be concluded that the bed-level predictions are not influenced by the mesh size.

The results provided by the unstructured grid give similar conclusions to those described in the 1D test case. Smart CFBS is the formula that provides the more accurate results. On the other hand, when comparing the numerical results obtained in 1D and 2D situations, it can be appreciated that in bidimensional situations, the error increases with independence of the employed formula. This is justified by the fact that in a 2D flow, the projections of the normal vector to the edge of each cell have to be taken into account. Furthermore, it is necessary to bear in mind the fact that the capacity formulae tested in this work are based on 1D experimental steady flows, so it is expected that these formulae provide less accurate results under 2D unsteady situations.

Dam break flow over an erodible bed (2D)

This experiment was designed at the laboratory of UCL (International Association for Hydro-Environment Engineering and Research Working Group (Soares-Frazao *et al.* 2012)). It is part of a benchmark test launched within the framework of the NSFPIRE project 'Modelling of Flood Hazards and Geomorphic Impacts of Levee Breach and Dam Failure'. It consists of a dam break over a 3.6 m wide and approximately 36 m long flume. The gate, located at $x = 0$ m, was connected to an upstream reservoir, and was 1 m wide. The sand was extended over 9 m downstream of the gate and 1 m upstream of the gate, with a thickness of

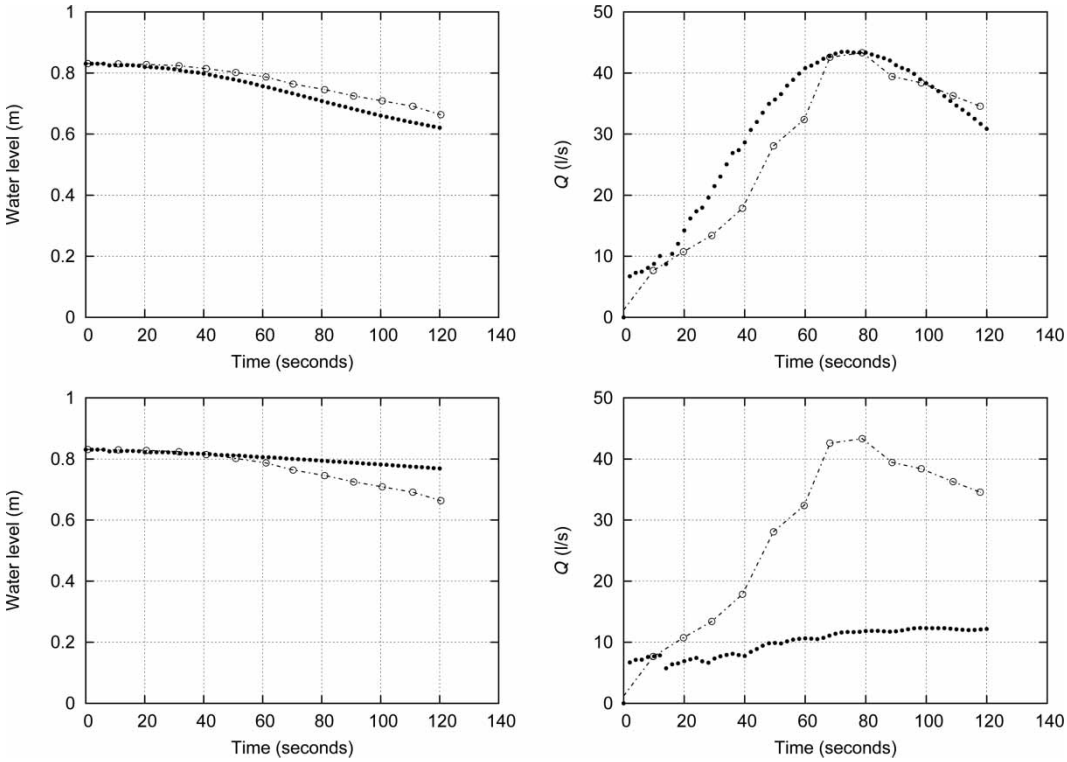

Figure 10 | Results obtained with Smart CFBS (upper) and MPM (lower) in the 1D case. Evolution in time of the measured water reservoir level (–○–) and computed water reservoir level (– • –) at $x = 0$ (left). Evolution in time of the measured (–○–) and computed (– • –) overtopping discharge (right).

0.085 m. A complete sketch of the experiment can be found in Soares-Frazao *et al.* (2012). The properties of the sand were $\rho_s = 2{,}630\ \mathrm{kg\,m^{-3}}$, $d_m = 1.61$ mm, $\varphi = 30^\circ$, negligible cohesion, porosity $p = 0.40$ and the roughness was characterized by a Manning factor $n = 0.019$. Initial conditions used were: upstream, the water level was imposed to

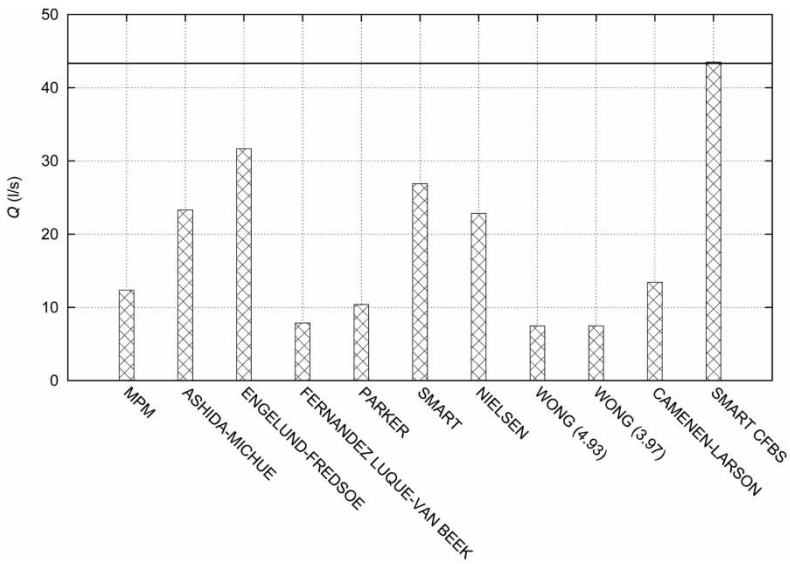

Figure 11 | Maximum overtopping discharge with different formulae in the 1D case.

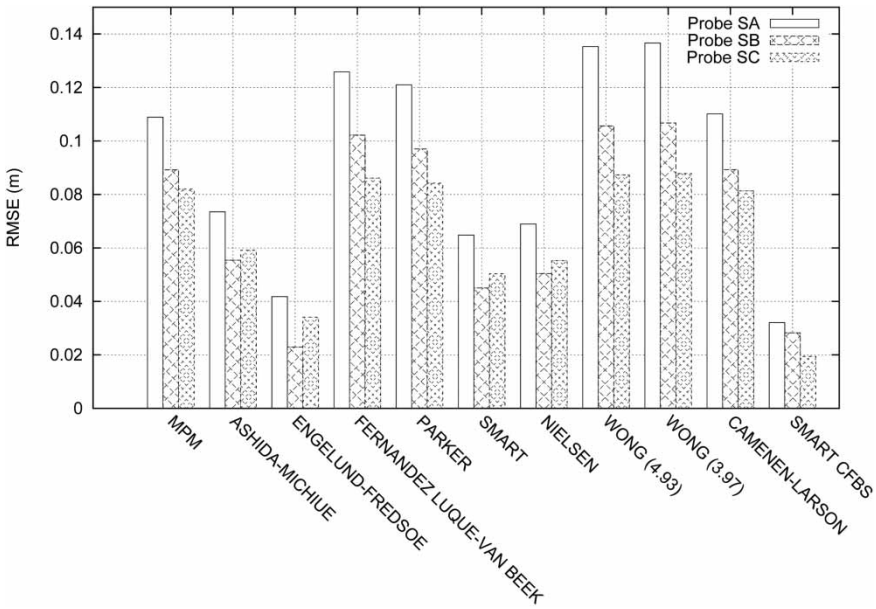

Figure 12 | RMSEs for bed level z with different formulae in the 1D case.

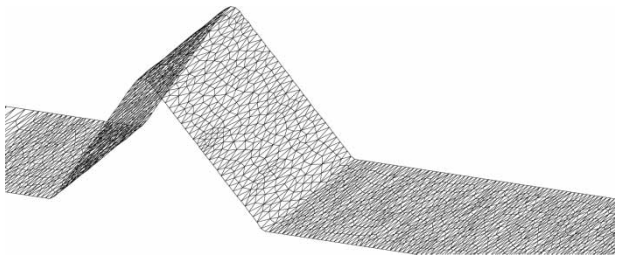

Figure 13 | Details of the 2D triangular mesh.

0.47 m, and downstream, a dry bed situation was imposed. At time $t = 100$ s, two longitudinal bed profiles were measured starting from $x = 0.5$ m at two y-coordinates: $y =$ 0.20 m (section S1) and $y = 0.70$ m (section S2). During the performance of this experiment, several runs were carried out. An average of the experimental results obtained during the runs was calculated. For comparison with the numerical results, this experimental average has been taken into account.

The domain was discretized on a non-uniform triangular mesh, with a higher density downstream of the widening, and with the finest cell size equal to 0.001 m^2.

Figure 17 shows a sequence in time of computed bed evolution plan views predicted by the Smart CFBS discretization. This sequence is characterized by fast

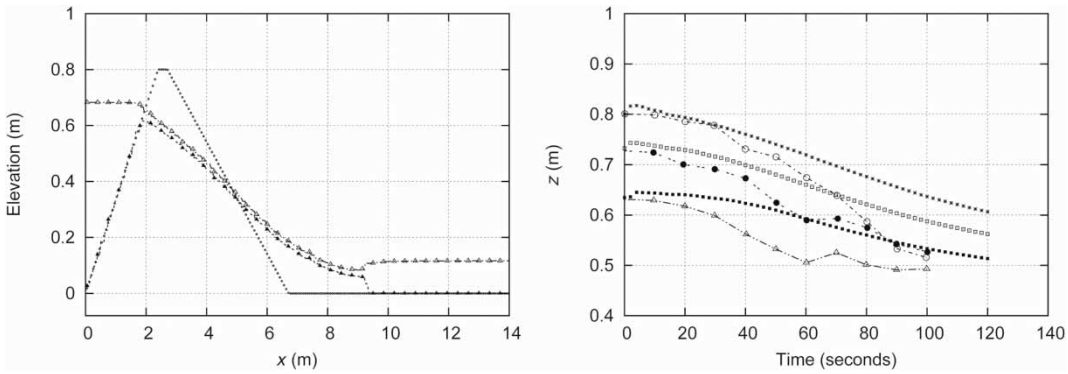

Figure 14 | Results obtained with Smart CFBS in the 2D case. Initial bed level (- - -), computed water-level surface (–△–) and bed-level surface (–▲–) at $t = 120$ s (left). Bed-level surface evolution in time measured at stations SA(–○–), SB (– ● –) and SC (–△–) and computed at stations SA (– ⋆ –), SB (––) and SC (–■–) (right).

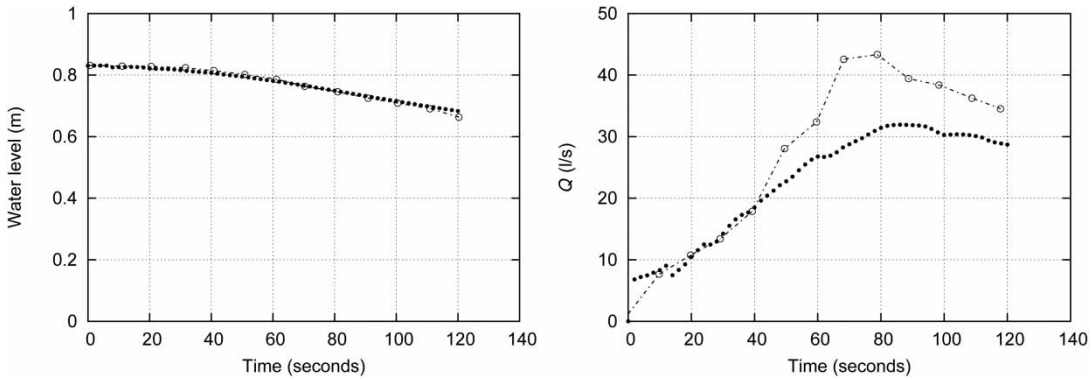

Figure 15 | Results obtained with Smart CFBS in the 2D case. Evolution in time of the measured water reservoir level (–○–) and computed water reservoir level (– • –) at $x = 0$ (left). Evolution in time of the measured (–○–) and computed (– • –) overtopping discharge (right).

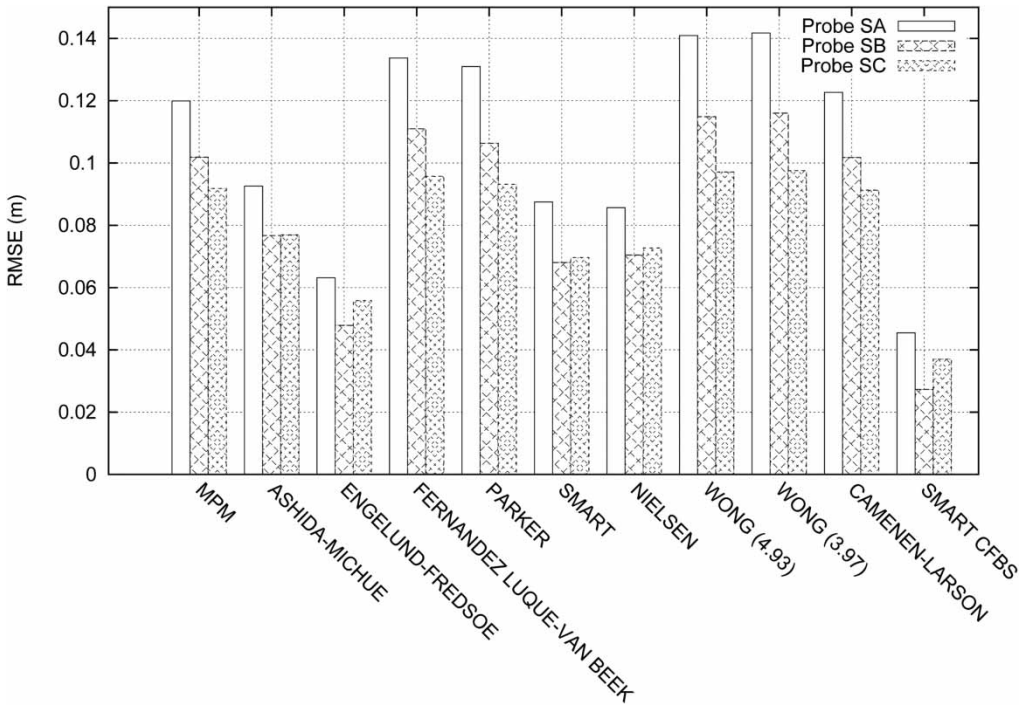

Figure 16 | RMSEs for bed level z with different formulae in the 2D case.

morphodynamic changes. Figure 17(a) at $t = 10$ s shows how the flow generates a wavefront that causes an important erosion process in the enlargement zone of the channel. While the flooding wave advances, the sand particles grabbed in this process are carried out to the wavefront and to the wall, where they tend to sediment, as shown in Figure 17(b) at $t = 20$ s. Symmetric elongated sedimentary bodies appear on the right and left banks of the channel, which grow in time to merge generating a diamond-shaped erosion region at $t = 40$ s, shown in Figure 17(c). At $t = 60$ s, most of the morphodynamic changes have taken place, and the drainage of the water contained in the upstream reservoir smooths the bed surface, attenuating the bed forms previously generated. For longer times, no more important morphodynamic changes happen. At $t = 100$ s, Figure 17(f) shows how only the diamond-shaped erosion region in the enlargement zone, generated by the sudden change in flow

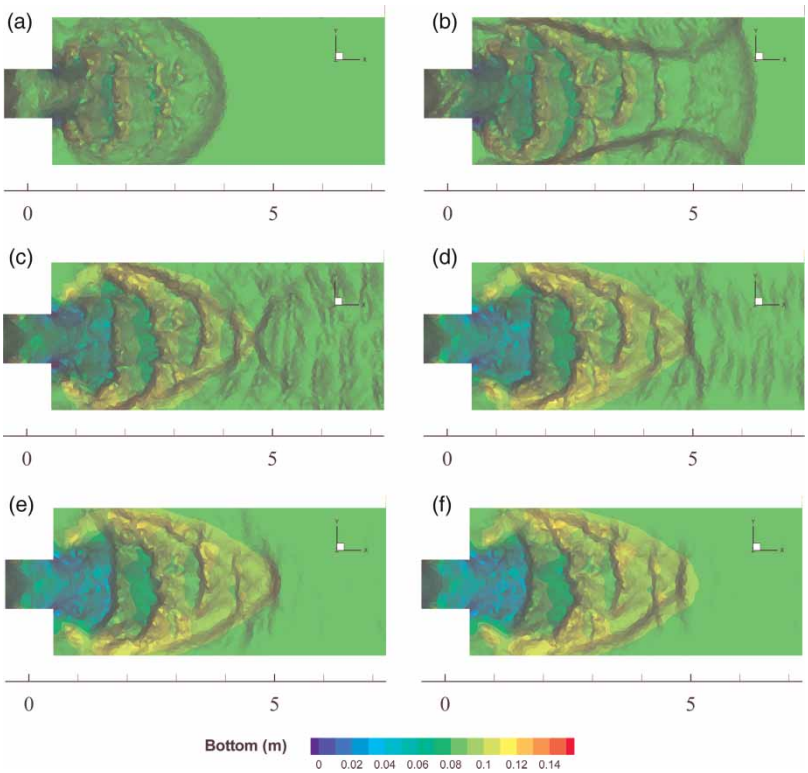

Figure 17 | Numerical results of bed level in the enlargement zone at 10s (a), 20s (b), 40s (c), 60s (d), 80s (e) and 100s (f) using the Smart CFBS formula.

direction after the opening of the gate, remains in time. The rest of the bed surface becomes almost planar.

The results shown in Figure 18 display the experimental bed level and the computed ones using the Smart CFBS and MPM formulae at the three cross sections, S1, S2 and S3. The profiles are cut off at $x = 4$ m because this zone is the most representative of the bed morphodynamic changes. The first one, section S1, placed to study the effect of the flow over the bottom in the enlargement zone, presents differences between both load discharge formulae. The Smart CFBS formula obtains a better tracking of the sedimentary process, getting more accurate results for the maximum erosion position, $x =$ 1.4 m, and in the maximum deposition position, $x = 3.5$ m.

At the second cross section, section S2, differences in the experimental results are also noticeable when using MPM and Smart CFBS formulae. The Smart CFSB formula provides an accurate prediction of the bed-level surface, leading to correct estimations of the maximum erosion at $x = 1.3$ m and of the deposition at $x = 3.5$ m. The computed results obtained with the MPM formula show a zone at $x =$ 1.2 m where erosion is clearly overestimated.

Finally, at the third section, section S3, which is placed in a position to study the effect of the wall roughness in the sedimentary process, the two formulations of sediment transport provide results totally different, both quite far away from the experimental values. This may be due to the fact that this numerical 2D model in the horizontal plane makes a depth average of the velocity gradient in the vertical plane, underestimating the erosion/deposition rates in the zone close to the wall. Hence, the model tends to smooth the results at that point. In this section, the MPM formula provides more accurate results than the Smart CFBS formula. This can be justified by the fact that in sections S1 and S2, the MPM formula predicts a bigger erosion rate than the Smart CFBS formulation, leading to an increase of deposition rate in the zone close to the wall, section S3.

The RMSEs of every section and every bed-load discharge are shown in Figure 19. The results obtained with the Smart CFBS formula are always among the ones that provide less error. The RMSEs obtained at section S3 are not shown, for the sake of clarity, due to the fact

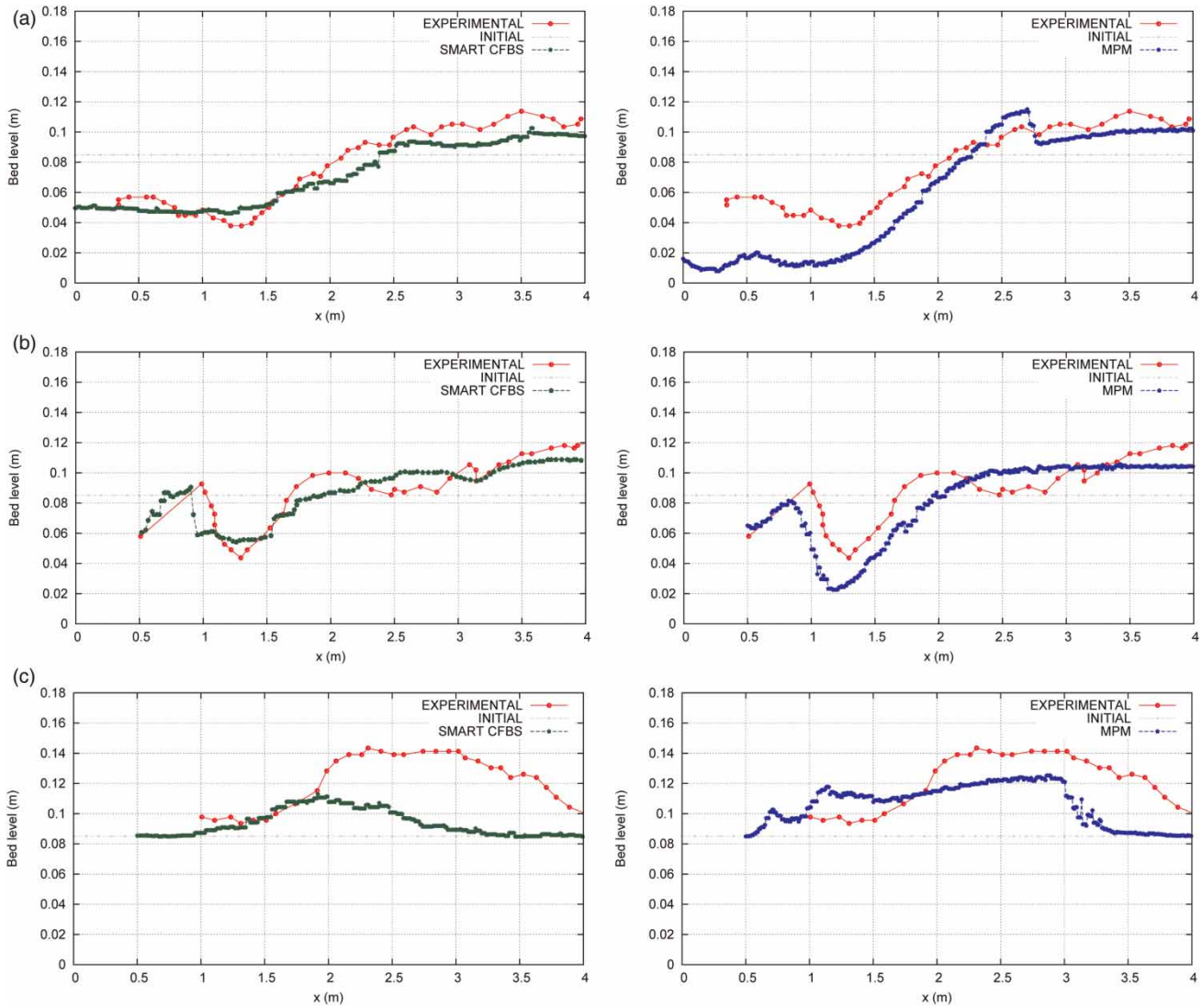

Figure 18 | Numerical results of bed level with Smart CFBS (left) and MPM (right) against experimental data at section S1 ($y = 0.2$ m) (a), at section S2 ($y = 0.7$ m) (b) and at section S3 ($y = 1.45$ m) (c) at $t = 100$ s.

that the numerical results are quite far away from the experimental data with all the formulae, as mentioned previously.

Dam break flow over an erodible channel with a sudden enlargement

A dam break over a dry and erodible bed experiment was performed at the laboratory of the Civil and Environmental Engineering Department of UCL (Palumbo *et al.* 2008; Goutiere *et al.* 2011), and is numerically reproduced here. This experiment allows the ability of the different empirical formulations and discretizations in a 2D flow configuration proposed in this work to be tested.

The upstream reservoir was 3 m long, and the total channel length was 6 m. The initial water depth upstream was set to 0.25 m, whilst the sediment layer was 0.1 m deep over the flume. A change in width was imposed 1 m downstream of the end of the reservoir, ranging from 0.25 to 0.5 m. A schematic sketch of the experimental set up is shown in Figure 20. The bed material was uniform sand with the following properties:

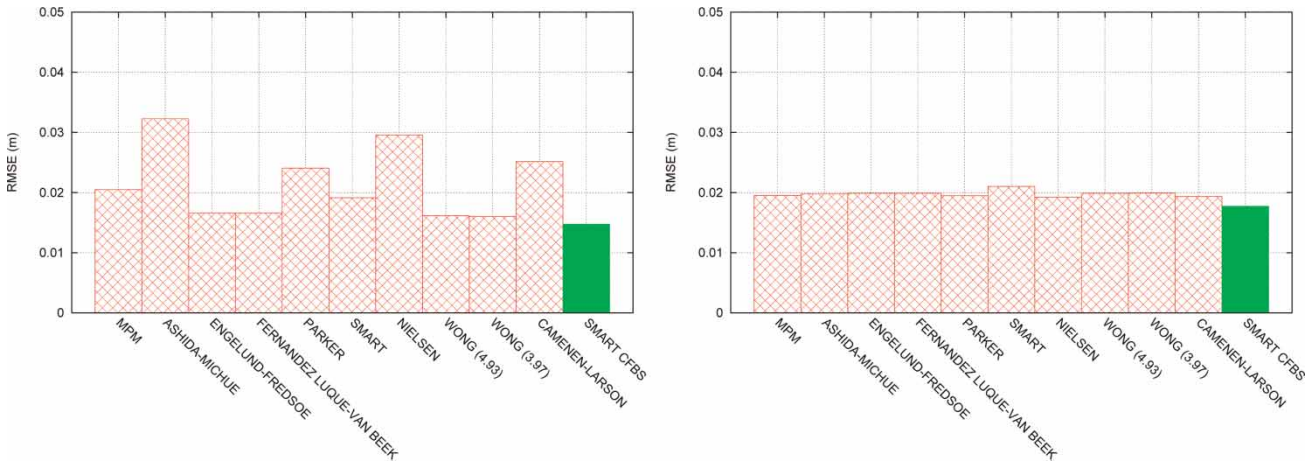

Figure 19 | RMSE values corresponding to the two cross sections, S1 (left) and S2 (right), and obtained with the considered sediment transport formulations.

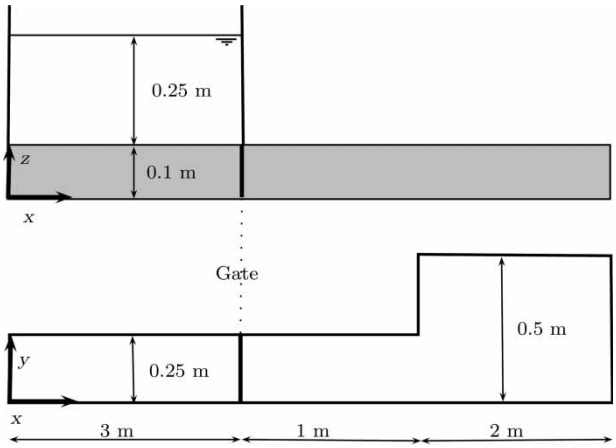

Figure 20 | Sketch of the experimental flume.

median diameter $d_m = 1.65$ mm, density $\rho_s = 2{,}630$ kg m^{-1}, friction angle $\varphi = 0.42^{\circ}$, negligible cohesion, porosity $p = 0.42$ and characterized by a Manning roughness factor $n = 0.0185$. The water-level evolution was measured at different points, whose locations are indicated in Table 2. The bed level was also recorded at specific sections at the end of the experiment, displayed in Table 3. Once the gate is opened, the flow remains 1D until it arrives at the enlargement zone, where the flow suffers a sudden change in its direction. The abrupt expansion generates a recirculating region and strong erosion at that point. The sand is transported and deposited on the left side of the channel.

The domain is discretized using a non-uniform triangular mesh of 4,300 triangles, locally refined downstream of the gate, as shown in Figure 21. The smallest cell area is approximately 0.001 m^2. The bed domain is considered deformable, and a free flow boundary condition is imposed at the domain exit.

Figure 22 displays several computed results at times 2 s (a), 3 s (b), 5 s (c) and 20 s (d), showing the bed-level surface. Most of the morphodynamic changes take place during the first 5 s of the dam break; Figures 22(a), (b) and (c). The erosion rate is of utmost importance at the corner of the enlargement zone, and is caused by the sudden change in flow velocity direction after the abrupt widening. A peak

Table 2 | Position of the probes

Probe	*x*-coordinate (m)	*y*-coordinate (m)
U1	3.75	0.125
U3	4.20	0.375
U6	4.95	0.125
U7	4.95	0.375

Table 3 | Position of the sections

Section	*x*-coordinate (m)
S1	4.10
S3	4.20
S5	4.30
S7	4.40
S9	4.50

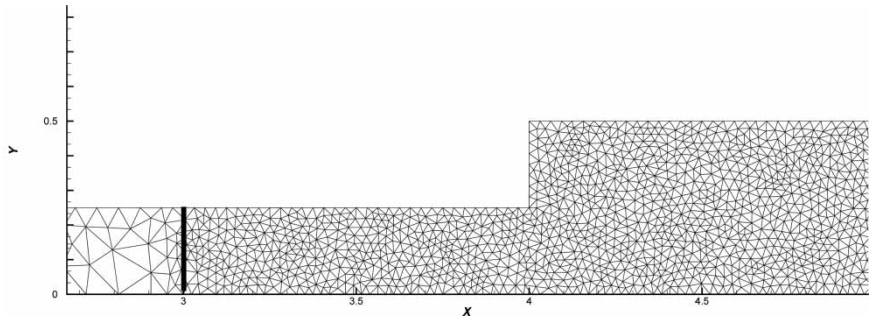

Figure 21 | Part of the triangular mesh. The gate is marked with a thick line at $x = 3$ m.

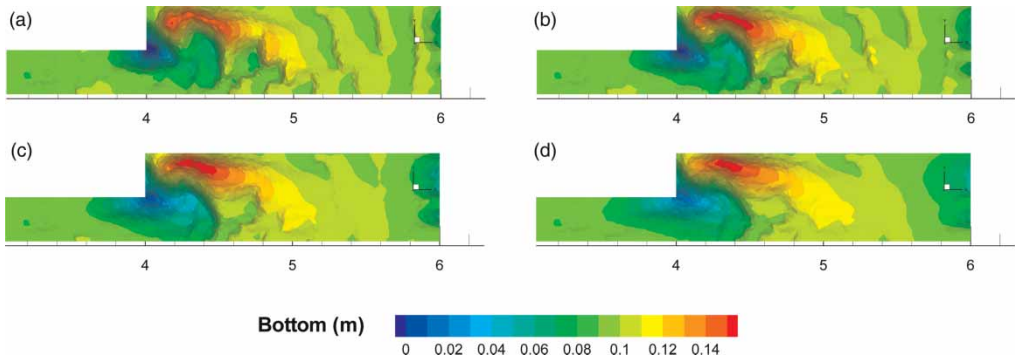

Figure 22 | Numerical results of water level (top image) and bed level (bottom level) in the enlargement zone at 2s (a), 3s (b), 5s (c) and 20s (d).

of material is formed at the left side of the channel. The sediment particles grabbed in this process are settled next to the right wall where the flow reduces its velocity. As a result of the bed deformation, an elongated sedimentary body appears on the right bank. At time $t = 20$ s (d), the initial strong erosion in the corner zone has been partially filled with sediment particles transported from the upstream zone. The rest of the bed-level surface does not change noticeably.

The experimental data and computational results for the water-level surface obtained with every sediment transport formula for each probe are displayed in Figure 23. Computed results at probe U1, which is placed within the channel, where the flow is mostly 1D, provided accurate results with respect to the experimental data. Numerical simulations at probe U3, located closer to the enlargement zone, where erosion is of maximum importance, reproduce less accurately the measured water surface level when compared with the rest of probes. Numerical results for probes U6 and U7 located downstream of the widening zone lead to accurate predictions of water-level surface. Numerical predictions using the MPM, Smart, Wong (3.97), Fernandez Luque & Van Beek and Smart CFBS formulae obtain closer results to the experimental data. The Smart formula provides less accurate results than the Smart CFBS one, although it does track the general trend of the temporal evolution.

The measured bed level after the dam break event and the numerical predictions at cross sections S1, S3, S5, S7 and S9 are plotted in Figures 24 (left) and 25 (left). The RMSEs obtained with every sediment transport discharge formula at cross sections S1, S3, S5, S7 and S9 are plotted in Figures 24 (right) and 25 (right).

All sediment transport formulations are able to describe the deposition of material on the left bank and the erosion on the right bank. More noticeable differences appear for the predicted bed level at the right bank, where deposition processes take place.

On the left bank ($y = 0$, looking upstream) of section S1, located close to the widening zone, all sediment transport formulations predict a bed profile that follows closely the pattern given by the experimental data. The Smart CFBS, Wong (4.93) and Wong (3.97) formulae provide the most accurate bed

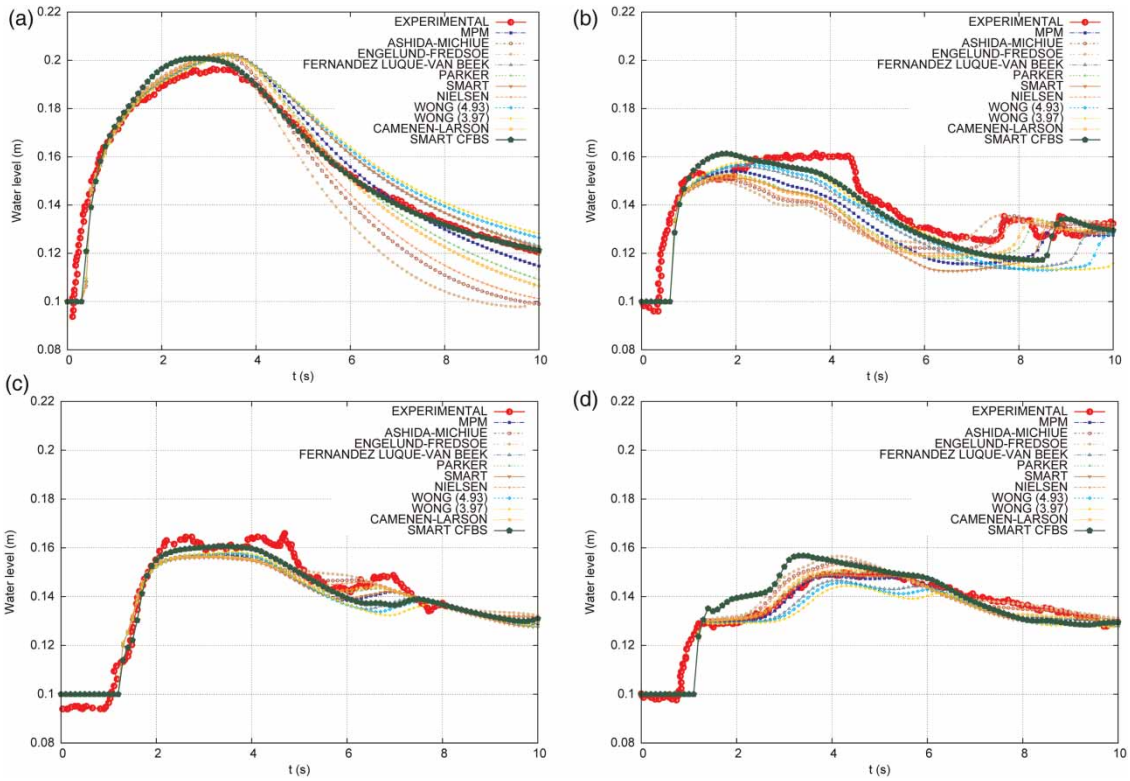

Figure 23 | Numerical results and experimental data of water level for probes U1 (a), U3 (b), U6 (c) and U7 (d).

elevations levels. For the right bank ($y = 0.5$), all formulations generate a less sharp slope than the one given by the experiments, and Wong (4.93) and Wong (3.97) also obtained the most accurate results. Sections S3 and S5 show that the numerical results track correctly the bed-level surface for both left and right banks, giving similar results and RMSE values. The Smart CFBS formula provides the least error. Section S7 shows that on the left bank, the level of erosion is well captured, with independence of the formulae. Noticeable differences among sediment discharge formulae appear in the stagnation flow region, located at the right wall, where the Smart CFBS formula obtained a better prediction for the bed-slope shape.

At Section S9, Figure 25, which is the cross section placed farthest from the enlargement location, numerical results give the lowest values of RMSEs. The bed level on the left bank is well tracked by all the formulations, but the key zone close to the right bank is only well predicted by the Smart CFBS, Wong (4.93) and Wong (3.97) formulae.

In order to check the ability of the numerical scheme used in this work to capture the bed-level evolution, the results for the Smart CFBS discretization are compared with those given by two other previously published mathematical models and numerical schemes. In these works, not all the sections were compared with the computed results obtained.

- The Catholic University of Louvain method (UCLM), where the 2D shallow-water equations and the Exner equation with the MPM formula as the closure relation are solved using a first-order Harten–Lax–Van Leer with contact discontinuities scheme (Soares-Frazao & Zech 2010).
- The Cardiff University method (UCM), where the set of equations includes a set of modified shallow-water equations, accounting for the sediment transport and bed deformation, non-equilibrium transport equations for suspended and bed loads, and an equation for bed evolution. The system of equations is solved using a spatially second-order Roe–monotone upstream centred schemes for conservation laws (Roe–MUSCL) scheme, described in Xia *et al.* (2010) and a bed-load formula proposed by Dou *et al.* (1999).

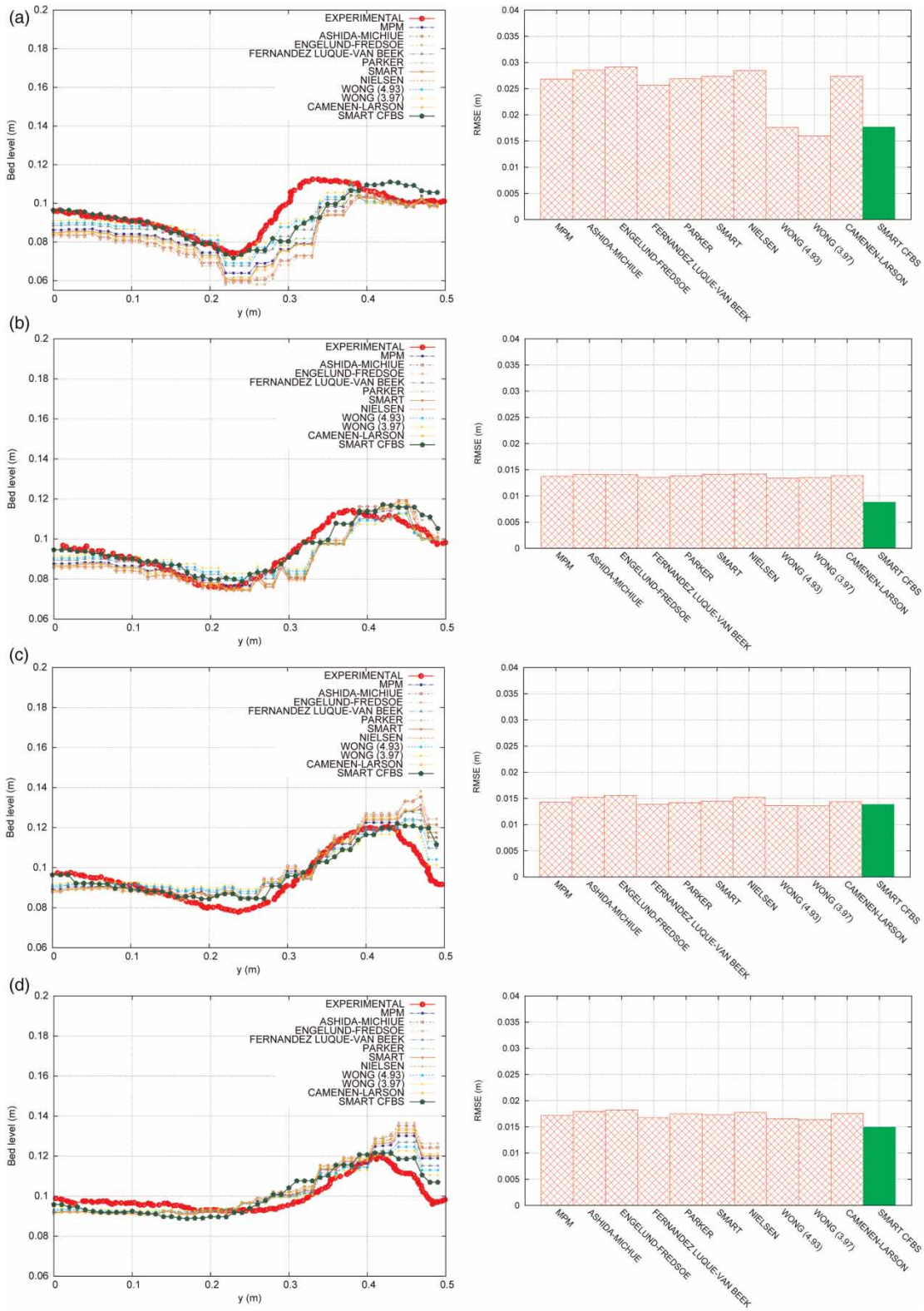

Figure 24 | Numerical results and experimental data of bed level for sections S1 (a), S3 (b), S5 (c), S7 (d), and corresponding RMSEs obtained with every sediment transport formula.

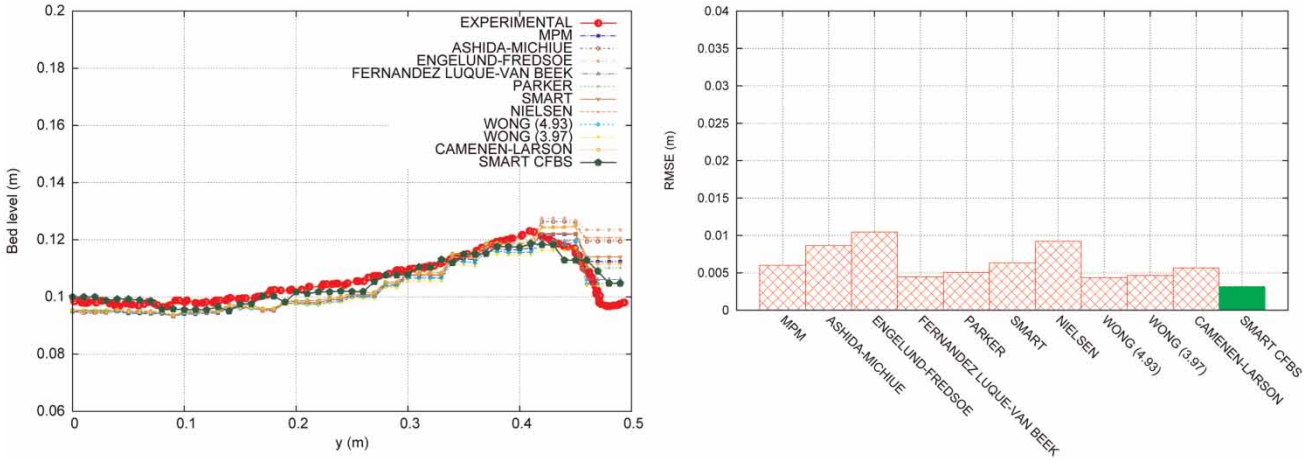

Figure 25 | Numerical results and experimental data of bed level for section S9, and corresponding RMSEs obtained with every sediment transport formula.

While the UCLM performed numerical simulations using a mesh with 30,000 unstructured triangles, the UCM presented results using an unstructured mesh with 8,100 triangular cells. In this comparison, the Smart CFBS results are generated using an unstructured triangular mesh with 4,300 cells. The spatial convergence of the numerical Smart CFBS results has not allowed noticeable differences when using finer meshes.

In Figure 26, experimental data of bed level and the numerical results computed by the Smart CFBS and UCLM schemes are compared in sections S3, S5 and S9. It can be noticed how the UCLM scheme tends to smooth the bed

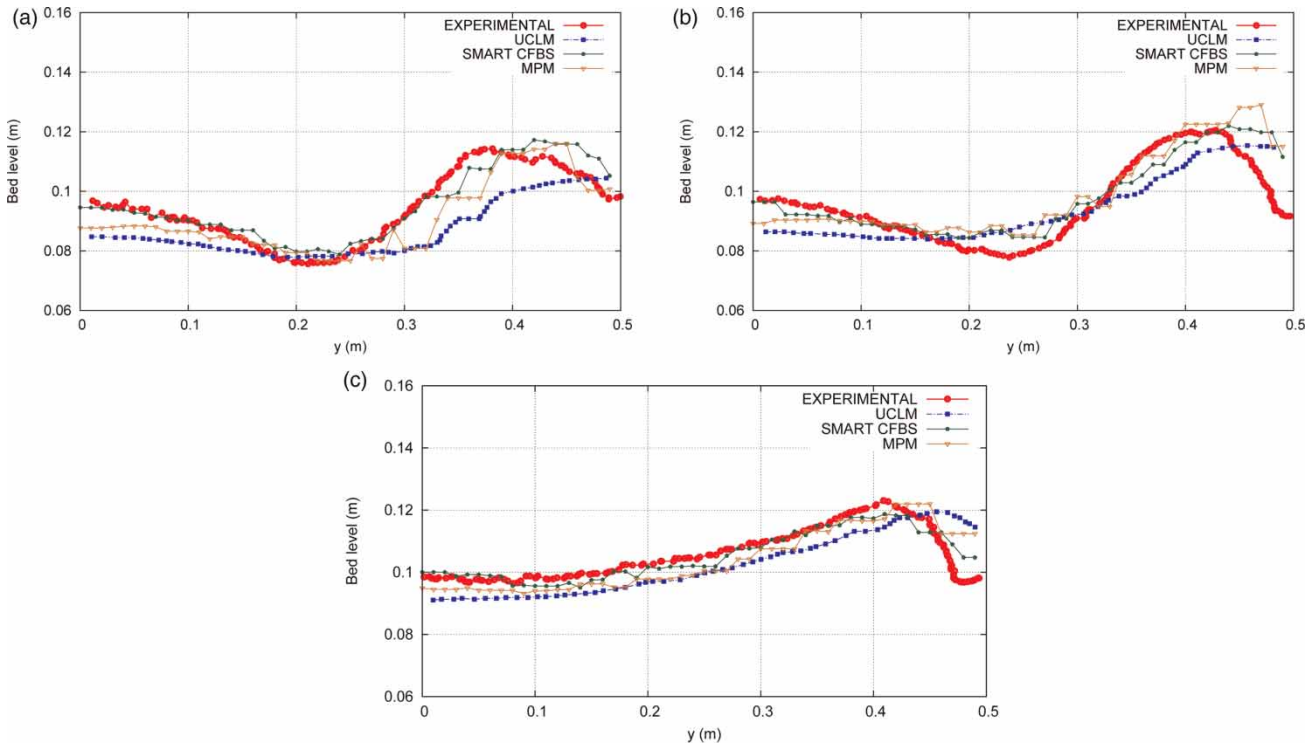

Figure 26 | Numerical results and experimental data of bed level for sections S3 (a), S5 (b) and S9 (c) with Smart CFBS, MPM and UCLM models.

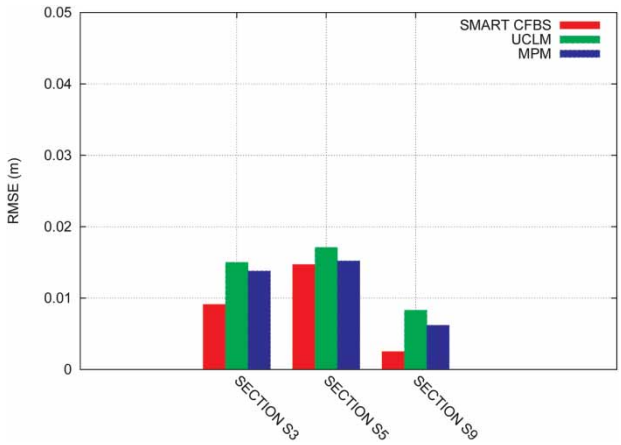

Figure 27 | RMSEs obtained with Smart CFBS, MPM and UCLM models at sections S3, S5 and S9.

morphology of the channel, as it is unable to reach neither the peak of erosion nor the peak of deposition. The characteristic form of the elongate tongue is lost. On the other hand, with the Smart CFBS formula, the evolution of the bed level is well tracked, the erosion effect on the left side and the deposition effect on the right side are correctly handled. It is worth noting the big difference in the quality of the results, despite the difference in the number of cells involved in each case. As the UCLM uses the MPM formula as closure for solid discharge, the results with our numerical model Murillo & García-Navarro (2010) considering also the MPM formula have been added to Figure 26. In this way, it is possible to see the part of the difference due to the formulation used and the part due to the other differences in the numerical model. It can be observed how the main profit in accuracy is due to the Smart CFBS formula. Figure 27 shows the RMSE associated with each model and with each bed-load discharge. The Smart CFBS formula provides the least error, and when comparing the UCLM and the MPM formulae together with the numerical scheme employed in this work, the RMSEs obtained with the numerical method presented in Murillo & García-Navarro (2010) provides the least errors.

Figure 28 displays the numerical results obtained with the Smart CFBS and UCM schemes for sections S1 and S7. The UCM tends to overestimate the scour in both sections, while generating an excessively planar bed surface. The Smart CFBS model provides better results than the UCM model for both sections.

The RMSEs calculated for the Smart CFBS and UCM methods are displayed in Figure 29, with similar errors associated with each one. On the other hand, as the UCM method is a spatially second-order Roe–MUSCL scheme, its computational cost should be significantly larger than the one obtained with a spatially first-order scheme, as for the one used in combination with the Smart CFBS method.

CONCLUSIONS

In this work, the Smart CFBS formula has been adapted from the original one in a non-trivial way. The bed slope in the original formula is replaced by the friction slope for zero or adverse slopes, and the bed slope is used for favourable slopes. This formulation is shown to be the best bed-load formula for transient morphological problems that involve 1D and 2D situations.

In the first set of test cases, the bed-load formulae have been applied to solve dam break flows over dry/wet initial conditions. In experiment A, over favourable slopes and a

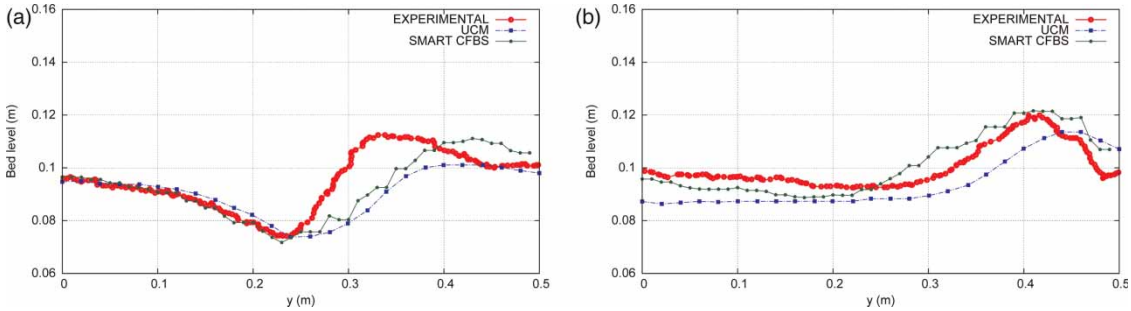

Figure 28 | Numerical results and experimental data of bed level for sections S1 (a) and S7 (b) with Smart CFBS and UCM models.

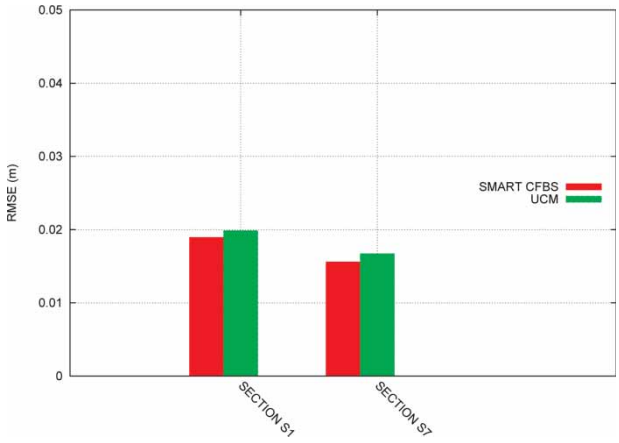

Figure 29 | RMSEs obtained with Smart CFBS and UCM models at sections S1 and S7.

dry bed, erosion produces a meaningful variation of the initial bed step, leading to a rate of erosion and deposition that is well captured in time and space using the Smart CFBS formula. In experiment B, where both sides are initially filled with water, and a favourable slope is present, the Smart CFBS formula leads to a correct erosion evolution in time. The RMSE calculated for all the formulae demonstrate the fact that Smart CFBS leads to minor computed errors in comparison with experimental data.

When numerically modelling dam erosion and failure, it has been found that the Smart CFBS formula is applicable in all the flow regimes present in the experiment. In addition, the Engelund & Fredsoe capacity formula provides correct results in bed-level predictions, although the Smart CFBS formula better estimates the maximum discharge value reached in the experiments. It is also worth mentioning that, for downstream steep slopes, the computational time associated with the peak discharge value was calculated earlier. When comparing the numerical results of the 2D simulation with those obtained for a 1D discretization, it can be observed that the RMSEs are slightly bigger in the 2D cases and the 2D results follow closely the tendencies given by the 1D formulation.

In the third experiment, a symmetric dam break over a mobile bed in a channel with an enlargement zone was numerically reproduced. In this case, a 2D flow was generated, and differences among different sediment formulations are less noticeable. Numerical results follow the tendency of the final bed morphology, underestimating the length of the diamond-shaped body and the thickness of the eroded layer. In the last experiment studied in this paper, where an erodible channel with a sudden enlargement produces a 2D flow, the computational results show good agreement with experimental values for the different sediment formulae. When comparing the results with the ones provided by other numerical schemes (UCLM and UCM), it is observed how the numerical method used in this work produces much less diffusive results for the bed forms, resulting in more accurate predictions. This diffusive effect is especially remarkable when comparing the results for the elongated sedimentary body that appears on the right bank. Furthermore, it is worth noting the fact that a coarser mesh is employed when using the Smart CFBS method, which gives less computational time.

Finally, although the Smart CFBS discretization reaches the most accurate results in all cases, in a genuinely 2D flow, that is, a situation involving more than one flow direction, the differences among sediment transport formulae are not as noticeable as in the 1D situations studied. This study has allowed a careful and detailed analysis of the relative behaviour to be performed in 2D situations of different sediment discharge formulae that were derived from 1D laboratory cases, and use of the Smart CFBS formula is suggested, regardless of the hydro-morphodynamic situation.

REFERENCES

Abderrezzak, K. K. & Paquier, A. 2011 Applicability of sediment transport capacity formulas to dam-break flows over movable beds. *Journal of Hydraulic Engineering* **137**, 209–221.

Ashida, K. & Michiue, M. 1972 Study on hydraulic resistance and bedload transport rate in alluvial streams. *Transactions, Japan Society of Civil Engineering* **206**, 569–589.

Begnudelli, L. & Sanders, F. 2006 Unstructured grid finite-volume algorithm for shallow-water flow and scalar transport with wetting and drying. *Journal of Hydraulic Engineering* **132**, 371–384.

Camenen, B. & Larson, M. 2005 A general formula for non-cohesive bed load sediment transport. *Journal of Estuarine, Coastal and Shelf Science* **63**, 249–260.

Campisano, A., Creaco, E. & Modica, C. 2004 Experimental and numerical analysis of the scouring effects of flushing waves on sediment deposits. *Journal of Hydrology* **299**, 324–334.

Cao, Z., Day, R. & Egashira, S. 2002 Coupled and decoupled numerical modeling of flow and morphological evolution

in alluvial rivers. *Journal of Hydraulic Engineering* **128**, 306–321.

Castro Diaz, M., Fernandez Nieto, E. & Ferreiro, A. 2008 Sediment transport models in shallow water equations and numerical approach by high order finite volume methods. *Journal of Computational Fluids* **37**, 299–316.

Creaco, E. & Bertrand-Krajewski, J. 2009 Numerical simulation of flushing effect on sewer sediments and comparison of four sediment transport formulae. *Journal of Hydraulic Research* **47** (2), 195–202.

Cunge, J., Holly, F. & Vervey, A. 1980 *Practical Aspects of Computational River Hydraulics*. Pitman, London.

De Vriend, H., Zyserman, J., Nicholson, J., Roelvink, J., Pechon, P. & Southgate, H. 1993 Medium-term 2dh coastal area modelling. *Journal of Coastal Engineering* **21**, 193–224.

Dou, X., Li, T. & Dou, G. 1999 Numerical model of total sediment transport in the Yangtze estuary. *China Ocean Engineering* **13**, 277–286.

Einstein, H. A. 1950 *The bed-load function for sediment transportation in open cannel flows*. Technical report 1026, US Department of Agriculture, Washington, DC, USA.

Engelund, F. & Fredsoe, J. 1976 Sediment transport model for straight alluvial channels. *Nordic Hydrology* **7** (5), 293–306.

Goutiere, L., Soares-Frazao, S. & Zech, Y. 2011 Dam-break flow on mobile bed in abruptly widening channel: experimental data. *Journal of Hydraulic Research* **49** (3), 367–371.

Grass, A. 1981 *Sediments Transport by Waves and Currents*. Department of Civil Engineering, University College, London.

Hudson, J. & Sweby, P. K. 2002 Formulations for numerically approximating hyperbolic systems governing sediment transport. *Journal of Scientific Computing* **19**, 225–251.

Juez, C., Murillo, J. & García-Navarro, P. 2012 Numerical discretization of the Exner equation in unsteady floods. In: *Proceedings of River Flow 2012, International Conference on Fluvial Hydraulics*, San José, Costa Rica.

Liu, X., Landry, B. & García, M. 2008 Two-dimensional scour simulations based on coupled model of shallow water equations and sediment transport on unstructured meshes. *Coastal Engineering* **55**, 800–810.

Luque, R. F. & van Beek, R. 1976 Erosion and transport of bedload sediment. *Journal of Hydraulics Research* **14**, 127–144.

Meyer-Peter, E. & Müller, R. 1948 Report on the 2nd Meeting International Association Hydraulic Structure Research. Stockholm, Sweden.

Murillo, J. & García-Navarro, P. 2010 An Exner-based coupled model for two-dimensional transient flow over erodible bed. *Journal of Computational Physics* **229**, 8704–8732.

Nielsen, P. 1992 *Coastal bottom, boundary layers and sediment transport*. Advanced Series on Ocean Engineering 4. World Scientific Publishing, Singapore.

Palumbo, A., Soares-Frazao, S., Goutiere, L., Pianese, D. & Zech, Y. 2008 Numerical discretization of the Exner equation in unsteady floods. In: *Proceedings of River Flow 2008, International Conference on Fluvial Hydraulics*, Cesme, Turkey.

Parker, G. 1979 Hydraulic geometry of active gravel rivers. *Journal of Hydraulic Engineering* **105** (9), 1185–1201.

Rosatti, G., Murillo, J. & Fraccarollo, L. 2007 Generalized roe schemes for 1d two-phase, free-surface flows over a mobile bed. *Journal of Computational Physics* **54**, 543–590.

Smart, G. 1984 Sediment transport formula for steep channels. *Journal of Hydraulic Engineering* **3**, 267–276.

Soares-Frazao, S. & Zech, Y. 2010 HLLC scheme with novel wave-speed estimators appropriate for two-dimensional shallow-water flow on erodible bed. *International Journal for Numerical Methods in Fluids* **66** (8), 1019–1036.

Soares-Frazao, S., Canelas, R., Cao, Z., Cea, L., Chaudhry, H., Moran, A., Kadi, K., Ferreira, R., Fraga-Cadorniga, I., Gonzalez-Ramirez, N., Greco, M., Huang, W., Imran, J., Coz, J. L., Marssoli, R., Paquier, A., Pender, G., Pontillo, M., Puertas, J., Spinewine, B., Swartenbroekx, C., Tsubaki, R., Villaret, C., Wu, W., Yue, Z. & Zech, Y. 2012 Dam-break flows over mobile beds: experiments and benchmark tests for numerical models. *Journal of Hydraulic Research* **50** (4), 364–375.

Spinewine, B. & Zech, Y. 2007 Small-scale laboratory dam-break waves on movable beds. *Journal of Hydraulic Research* **45**, 73–86.

Tingsanchali, T. & Chinnarasri, C. 2001 Numerical modelling of dam failure due to flow overtopping. *Hydrological Sciences Journal – Journal des Sciences Hydrologiques* **46**, 113–130.

Whittaker, J. & Davies, T. 1982 Erosion and sediment transport processes in step-pool torrents. *Hydrological Sciences Journal – Journal des Sciences Hydrologiques* **27** (2), 234–244.

Wong, M. 2003 Does the bedload transport relation of Meyer-peter and Müller fits its own data? In: *Proceedings of 30th IAHR-Congress*, Thessaloniki, Greece.

Wu, W. & Wang, S. 2004 Depth averaged two dimensional numerical modelling of unsteady flow and non uniform sediment transport in open channels. *Journal of Hydraulic Engineering* **130**, 1013–1024.

Wu, W. & Wang, S. 2007 One-dimensional modeling of dam-break flow over movable beds. *Journal of Hydraulic Engineering* **133**, 48–58.

Xia, J., Lin, B., Falconer, R. & Wang, G. 2010 Modelling dam-break flows over mobile beds using a 2d coupled approach. *Advances in Water Resources* **33**, 171–183.

First received 20 September 2012; accepted in revised form 12 February 2013. Available online 29 March 2013